

RESEARCH ARTICLE

# Computational mechanisms underlying cortical responses to the affordance properties of visual scenes

Michael F. Bonner\*, Russell A. Epstein

Department of Psychology, University of Pennsylvania, Philadelphia, PA, United States of America

\* [michafra@sas.upenn.edu](mailto:michafra@sas.upenn.edu)



## Abstract

Biologically inspired deep convolutional neural networks (CNNs), trained for computer vision tasks, have been found to predict cortical responses with remarkable accuracy. However, the internal operations of these models remain poorly understood, and the factors that account for their success are unknown. Here we develop a set of techniques for using CNNs to gain insights into the computational mechanisms underlying cortical responses. We focused on responses in the occipital place area (OPA), a scene-selective region of dorsal occipitoparietal cortex. In a previous study, we showed that fMRI activation patterns in the OPA contain information about the navigational affordances of scenes; that is, information about where one can and cannot move within the immediate environment. We hypothesized that this affordance information could be extracted using a set of purely feedforward computations. To test this idea, we examined a deep CNN with a feedforward architecture that had been previously trained for scene classification. We found that responses in the CNN to scene images were highly predictive of fMRI responses in the OPA. Moreover the CNN accounted for the portion of OPA variance relating to the navigational affordances of scenes. The CNN could thus serve as an image-computable candidate model of affordance-related responses in the OPA. We then ran a series of *in silico* experiments on this model to gain insights into its internal operations. These analyses showed that the computation of affordance-related features relied heavily on visual information at high-spatial frequencies and cardinal orientations, both of which have previously been identified as low-level stimulus preferences of scene-selective visual cortex. These computations also exhibited a strong preference for information in the lower visual field, which is consistent with known retinotopic biases in the OPA. Visualizations of feature selectivity within the CNN suggested that affordance-based responses encoded features that define the layout of the spatial environment, such as boundary-defining junctions and large extended surfaces. Together, these results map the sensory functions of the OPA onto a fully quantitative model that provides insights into its visual computations. More broadly, they advance integrative techniques for understanding visual cortex across multiple level of analysis: from the identification of cortical sensory functions to the modeling of their underlying algorithms.

## OPEN ACCESS

**Citation:** Bonner MF, Epstein RA (2018) Computational mechanisms underlying cortical responses to the affordance properties of visual scenes. *PLoS Comput Biol* 14(4): e1006111. <https://doi.org/10.1371/journal.pcbi.1006111>

**Editor:** Wolfgang Einhäuser, Technische Universität Chemnitz, GERMANY

**Received:** August 18, 2017

**Accepted:** March 31, 2018

**Published:** April 23, 2018

**Copyright:** © 2018 Bonner, Epstein. This is an open access article distributed under the terms of the [Creative Commons Attribution License](https://creativecommons.org/licenses/by/4.0/), which permits unrestricted use, distribution, and reproduction in any medium, provided the original author and source are credited.

**Data Availability Statement:** Data and stimuli are available at: <https://figshare.com/s/5ff0a04c2872e1e1f416>.

**Funding:** This work was supported by US NIH grant EY-022350 (RAE). The funders had no role in study design, data collection and analysis, decision to publish, or preparation of the manuscript.

**Competing interests:** The authors have declared that no competing interests exist.

## Author summary

How does visual cortex compute behaviorally relevant properties of the local environment from sensory inputs? For decades, computational models have been able to explain only the earliest stages of biological vision, but recent advances in deep neural networks have yielded a breakthrough in the modeling of high-level visual cortex. However, these models are not explicitly designed for testing neurobiological theories, and, like the brain itself, their internal operations remain poorly understood. We examined a deep neural network for insights into the cortical representation of navigational affordances in visual scenes. In doing so, we developed a set of high-throughput techniques and statistical tools that are broadly useful for relating the internal operations of neural networks with the information processes of the brain. Our findings demonstrate that a deep neural network with purely feedforward computations can account for the processing of navigational layout in high-level visual cortex. We next performed a series of experiments and visualization analyses on this neural network. These analyses characterized a set of stimulus input features that may be critical for computing navigationally related cortical representations, and they identified a set of high-level, complex scene features that may serve as a basis set for the cortical coding of navigational layout. These findings suggest a computational mechanism through which high-level visual cortex might encode the spatial structure of the local navigational environment, and they demonstrate an experimental approach for leveraging the power of deep neural networks to understand the visual computations of the brain.

## Introduction

Recent advances in the use of deep neural networks for computer vision have yielded image computable models that exhibit human-level performance on scene- and object-classification tasks [1–4]. The units in these networks often exhibit response profiles that are predictive of neural activity in mammalian visual cortex [5–11], suggesting that they might be profitably used to investigate the computational algorithms that underlie biological vision [12–16]. However, many of the internal operations of these models remain mysterious, and the fundamental theoretical principles that account for their predictive accuracy are not well understood [16–18]. This presents an important challenge to the field: if deep neural networks are to fulfill their potential as a method for investigating visual perception in living organisms, it will first be necessary to develop techniques for using these networks to provide computational insights into neurobiological systems.

It is this issue—the use of deep neural networks for gaining insights into the computational processes of biological vision—that we address here. We focus in particular on the mechanisms underlying natural scene perception. A central aspect of scene perception is the identification of the *navigational affordances* of the local environment—where one can move to (e.g., a doorway or an unobstructed path), and where one’s movement is blocked. In a recent fMRI study, we showed that the navigational-affordance structure of scenes could be decoded from multivoxel response patterns in scene-selective visual areas [19]. The strongest results were found in a region of the dorsal occipital lobe known as the occipital place area (OPA), which is one of three patches of high-level visual cortex that respond strongly and preferentially to images of spatial scenes [20–24]. These results demonstrated that the OPA encodes affordance-related visual features. However, they did not address the crucial question of how these features might be computed from sensory inputs.

There was one aspect of the previous study that provided a clue as to how affordance representations might be constructed: affordance information was present in the OPA even though participants performed tasks that made no explicit reference to this information. For example, in one experiment, participants were simply asked to report the colors of dots overlaid on the scene, and in another experiment, they were asked to perform a category-recognition task. Despite the fact that these tasks did not require the participants to think about the spatial layout of the scene or plan a route through it, it was possible to decode navigational affordances in the OPA in both cases. This suggested to us that affordances might be rapidly and automatically extracted through a set of purely feedforward computations.

In the current study we tested this idea by examining a biologically inspired CNN with a feedforward architecture that was previously trained for scene classification [3]. This CNN implements a hierarchy of linear-nonlinear operations that give rise to increasingly complex feature representations, and previous work has shown that its internal representations can be used to predict neural responses to natural scene images [25, 26]. It has also been shown that the higher layers of this CNN can be used to decode the coarse spatial properties of scenes, such as their overall size [25]. By examining this CNN, we aimed to demonstrate that affordance information could be extracted by a feedforward system, and to better understand how this information might be computed.

To preview our results, we find that the CNN contains information about fine-grained spatial features that could be used to map out the navigational pathways within a scene; moreover, these features are highly predictive of affordance-related fMRI responses in the OPA. These findings demonstrate that the CNN can serve as a candidate, image-computable model of navigational-affordance coding in the human visual system. Using this quantitative model, we then develop a set of techniques that provide insights into the computational operations that give rise to affordance-related representations. These analyses reveal a set of stimulus input features that are critical for predicting affordance-related cortical responses, and they suggest a set of high-level, complex features that may serve as a basis set for the population coding of navigational affordances. By combining neuroimaging findings with a fully quantitative computational model, we were able to complement a theory of cortical representation with discoveries of its algorithmic implementation—thus providing insights at multiple levels of understanding and moving us toward a more comprehensive functional description of visual cortex.

## Results

### Representation of navigational affordances in scene-selective visual cortex

To test for the representation of navigational affordances in the human visual system, we examined fMRI responses to 50 images of indoor environments with clear navigational paths passing through the bottom of the scene (Fig 1A). Subjects viewed these images one at a time for 1.5 s each while maintaining central fixation and performing a category-recognition task that was unrelated to navigation (i.e., press a button when the viewed scene was a bathroom). Details of the experimental paradigm and a complete analysis of the fMRI responses can be found in a previous report [19]. In this section, we briefly recapitulate the aspects of the results that are most relevant to the subsequent computational analyses.

To measure the navigational affordances of these stimuli, we asked an independent group of subjects to indicate with a computer mouse the paths that they would take to walk through each environment starting from the bottom of the image (Fig 1B). From these responses, we created probabilistic maps of the navigational paths through each scene. We then constructed histograms of these navigational probability measurements in one-degree angular bins over a range of directions radiating from the starting point of the paths. These histograms

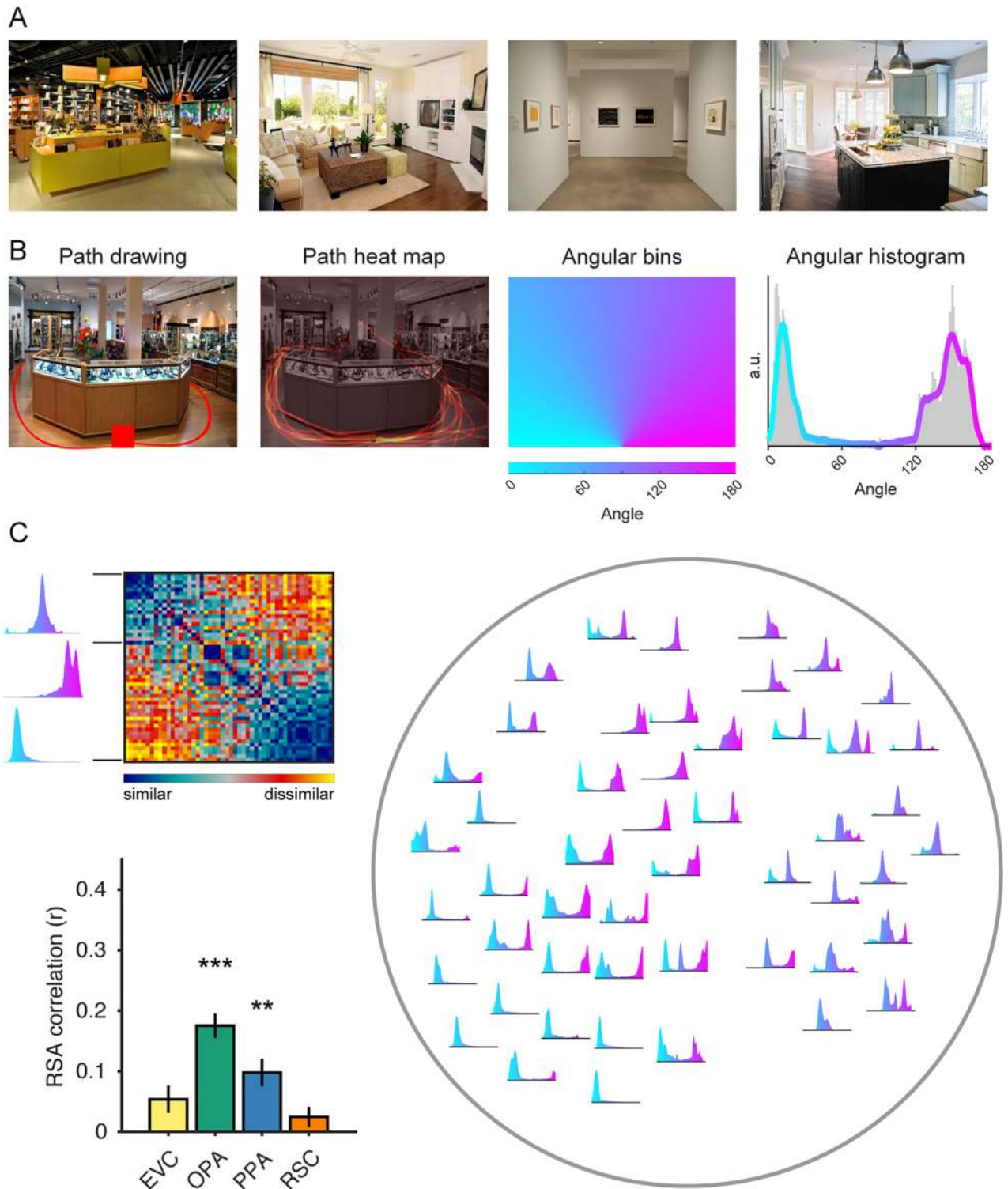


**Fig 1. Navigational-affordance information is coded in scene-selective visual cortex.** (A) Examples of natural images used in the fMRI experiment. All experimental stimuli were images of indoor environments with clear navigational paths proceeding from the bottom center of the image. (B) In a norming study, an independent group of raters indicated with a computer mouse the paths that they would take to walk through each scene, starting from the red square at the bottom center of the image (far left panel). These data were combined across subjects to create heat maps of the navigational paths in each image (middle left panel). We summed the values in these maps along one-degree angular bins radiating from the bottom center of the image (middle right panel), which produced histograms of navigational probability measurements over a range of angular directions (far right panel). The gray bars in this histogram represent raw data, and the overlaid line indicates the angular data after smoothing. (C) The navigational

histograms were compared pairwise across all images to create a model RDM of navigational-affordance coding (top left panel). Right panel shows a two-dimensional visualization of this representational model, created using t-distributed stochastic neighbor embedding (t-SNE), in which the navigational histograms for each condition are plotted within the two-dimensional embedding. RSA correlations were calculated between the model RDM and neural RDMs for each ROI (bottom left panel). The strongest RSA effect for the coding of navigational affordances was in the OPA. There was also a significant effect in the PPA. Error bars represent bootstrap  $\pm 1$  s.e.m. a.u. = arbitrary units. \*\* $p < 0.01$ , \*\*\* $p < 0.001$ .

<https://doi.org/10.1371/journal.pcbi.1006111.g001>

approximate a probabilistic affordance map of potential navigational paths radiating from the perspective of the viewer [27].

We then tested for the presence of affordance-related information in fMRI responses using representational similarity analysis (RSA) [28]. In RSA, the information encoded in brain responses is compared with a cognitive or computational model through correlations of their representational dissimilarity matrices (RDMs). RDMs are constructed through pairwise comparisons of the model representations or brain responses for all stimulus classes (in this case, the 50 images), and they serve as a summary measurement of the stimulus-class distinctions. The correlation between any two RDMs reflects the degree to which they contain similar information about the stimuli. We constructed an RDM for the navigational-affordance model through pairwise comparisons of the affordance histograms (Fig 1C). Neural RDMs were constructed for several regions of interest (ROIs) through pairwise comparisons of their multivoxel activation patterns for each image.

We focused our initial analyses on three ROIs that are known to be strongly involved in scene processing: the OPA, the parahippocampal place area (PPA), and the retrosplenial complex (RSC) [20–24]. All three of these regions respond more strongly to spatial scenes (e.g., images of landscapes, city streets, or rooms) than other visual stimuli, such as objects and faces, and thus are good candidates for supporting representations of navigational affordances. We also examined patterns in early visual cortex (EVC). Using RSA to compare the RDMs for these regions to the navigational-affordance RDM, we found evidence that affordance information is encoded in scene-selective visual cortex, most strongly in the dorsal scene-selective region known as the OPA (Fig 1C). These effects were not observed in lower-level EVC, suggesting that navigational affordances likely reflect mid-to-high-level visual features that require several computational stages along the cortical hierarchy. In our previous report, a whole-brain searchlight analysis confirmed that the strongest cortical locus of affordance coding overlapped with the OPA [19]. Interestingly, affordance coding in scene regions was observed even though participants performed a perceptual-semantic recognition task in which they were not explicitly asked about the navigational affordances of the scene—suggesting that affordance information is automatically elicited during scene perception. Together, these results suggest that scene-selective visual cortex routinely encodes complex spatial features that can be used to map out the navigational affordances of the local visual scene.

These analyses provide functional insights into visual cortex at the level of representation—that is, the identification of sensory information encoded in cortical responses. However, an equally important question for any theory of sensory cortical function is to understand *how* its representations can be computed at an algorithmic level [12–16]. Understanding the algorithms that give rise to high-level sensory representations requires a quantitative model that implements representational transformations from visual stimuli. Thus, we next turn to the question of how affordance representations might be computed from sensory inputs.

## Explaining affordance-related cortical representations with a feedforward image-computable model

Visual cortex implements a complex set of highly nonlinear transformations that remain poorly understood. Attempts at modeling these transformations using hand-engineered



algorithms have long fallen short of accurately predicting mid-to-high-level sensory representations [6, 10, 11, 29–31]. However, advances in the development of artificial deep neural networks have dramatically changed the outlook for the quantitative modeling of visual cortex. In particular, recently developed deep CNNs for tasks such as image classification have been found to predict sensory responses throughout much of visual cortex at an unprecedented level of accuracy [5–11]. The performance of these CNNs suggests that they hold the promise of providing fundamental insights into the computational algorithms of biological vision. However, because their internal representations were not hand-engineered to test specific theoretical operations, they are challenging to interpret. Indeed, most of the critical parameters in CNNs are set through supervised learning for the purpose of achieving accurate performance on computer vision tasks, meaning that the resulting features are unconstrained by *a priori* theoretical principles. Furthermore, the complex transformations of these internal CNN units cannot be understood through a simple inspection of their learned parameters. Thus, neural network models have the potential to be highly informative to sensory neuroscience, but a critical challenge for moving forward is the development of techniques to probe the factors that best account for similarities between cortical responses and the internal representations of the models.

Here we tested a deep CNN as a potential candidate model of affordance-related responses in scene-selective visual cortex. Given the apparent automaticity of affordance-related responses, we hypothesized that they could be modeled through a set of purely feedforward computations performed on image inputs. To test this idea, we examined a model that was previously trained to classify images into a set of scene categories [3]. This feedforward model contains 5 convolutional layers followed by 3 fully connected layers, the last of which contains units corresponding to a set of scene category labels (Fig 2A). The architecture of the model is similar to the AlexNet model that initiated the recent surge of interest in CNNs for computer vision [2]. Units in the convolutional layers of this model have local connectivity, giving rise to increasingly large spatial receptive fields from layers 1 through 5. The dense connectivity of the final three layers means that the selectivity of their units could depend on any spatial position in the image. Each unit in the CNN implements a linear-nonlinear operation in which it computes a weighted linear sum of its inputs followed by a nonlinear activation function (specifically, a rectified linear threshold). The weights on the inputs for each unit define a type of filter, and each convolutional layer contains a set of filters that are replicated with the same set of weights over all parts of the image (hence the term “convolution”). There are two other non-linear operations implemented by a subset of the convolutional layers: max-pooling, in which only the maximum activation in a local pool of units is passed to the next layer, and normalization, in which activations are adjusted through division by a factor that reflects the summed activity of multiple units at the same spatial position. Together, this small set of functional operations along with a set of architectural constraints define an untrained model whose many other parameters can be set through gradient descent with backpropagation—producing a trained model that performs highly complex feats of visual classification.

We passed the images from the fMRI experiment through the CNN and constructed a set of RDMs using the final outputs from each layer. We then used RSA to compare the representations of the CNN with: (i) the RDM for the navigational-affordance model and (ii) the RDM for fMRI responses in the OPA. The RSA comparisons with the affordance model showed that the CNN contained affordance-related information, which arose gradually across the lower layers and peaked in layer 5, the highest convolutional layer (Fig 2B). Note that this was the case despite the fact that the CNN was trained to classify scenes based on their categorical identity (e.g., kitchen), not their affordance structure. Weak effects were observed in lower convolutional layers, consistent with the pattern of findings from the fMRI experiment, in which

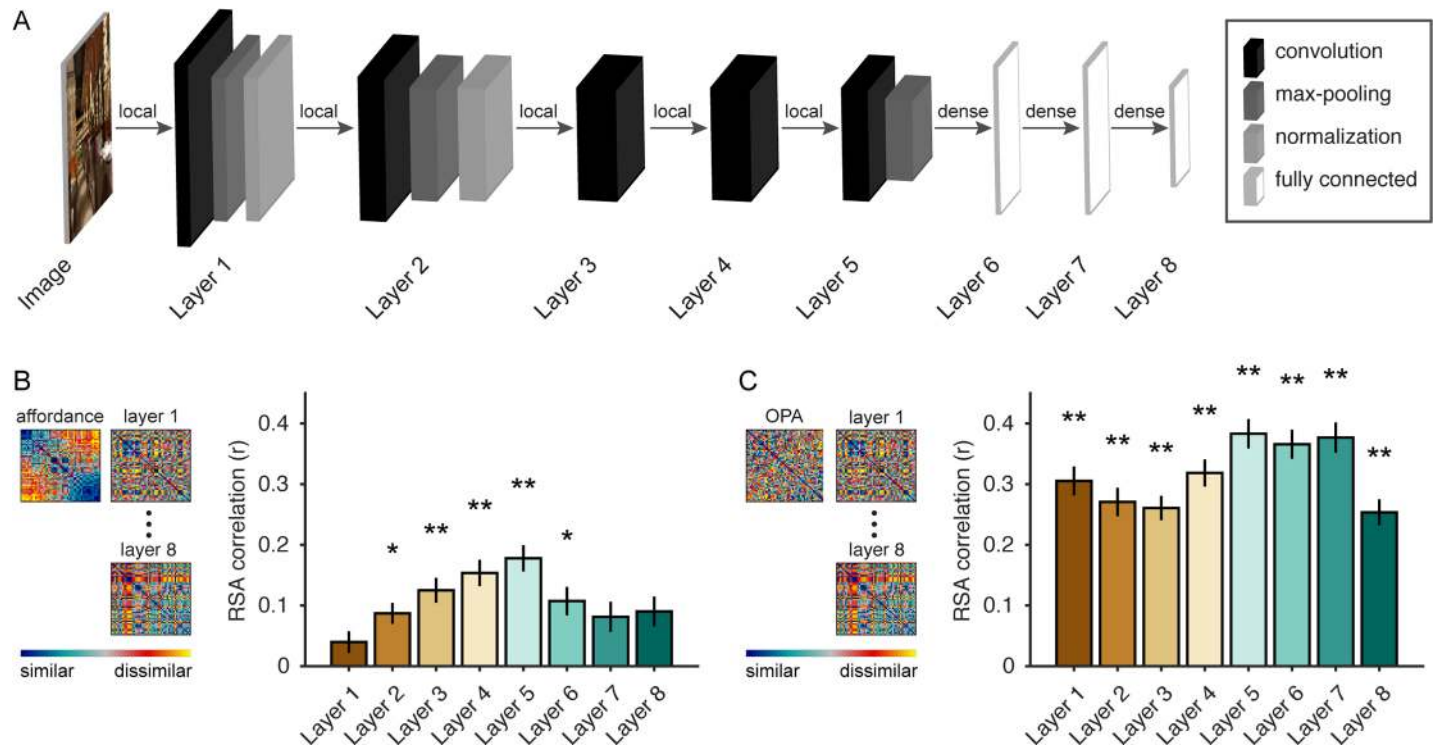


**Fig 2. Navigational-affordance information can be extracted by a feedforward computational model.** (A) Architecture of a deep CNN trained for scene categorization. Image pixel values are passed to a feedforward network that performs a series of linear-nonlinear operations, including convolution, rectified linear activation, local max pooling, and local normalization. The final layer contains category-detector units that can be interpreted as signaling the association of the image with a set of semantic labels. (B) RSA of the navigational-affordance model and the outputs from each layer of the CNN. The affordance model correlated with multiple layers of the CNN, with the strongest effects observed in higher convolutional layers and weak or no effects observed in the earliest layers. This is consistent with the findings of the fMRI experiment, which indicate that navigational affordances are coded in mid-to-high-level visual regions but not early visual cortex. (C) RSA of responses in the OPA and the outputs from each layer of the CNN. All layers showed strong RSA correlations with the OPA, and the peak correlation was in layer 5, the highest convolutional layer. Error bars represent bootstrap  $\pm 1$  s.e.m. \* $p < 0.05$ , \*\* $p < 0.01$ .

<https://doi.org/10.1371/journal.pcbi.1006111.g002>

affordance representations were not evident in EVC, and they suggest that affordances reflect mid-to-high-level, rather than low-level, visual features. The decrease in affordance-related information in the last three fully connected layers may result from the increasingly semantic nature of representations in these layers, which ultimately encode a set of scene-category labels that are likely unrelated to the affordance-related features of the scenes. The RSA comparisons with OPA responses showed that the CNN provided a highly accurate model of representations in this brain region, with strong effects across all CNN layers and a peak correlation in layer 5 (Fig 2B). Indeed, several layers of the CNN reached the highest accuracy we could expect for any model, given the noise ceiling of the OPA, which was calculated from the variance across subjects ( $r$ -value for OPA noise ceiling = 0.30). Together, these findings demonstrate the feasibility of computing complex affordance-related features through a set of purely feedforward transformations, and they show that the CNN is a highly predictive model of OPA responses to natural images depicting such affordances.

The above findings demonstrate that the CNN is representationally similar to the navigational-affordance RDM and also similar to the OPA RDM, but they leave open the important question of whether the CNN captures the same variance in the OPA as the navigational-affordance RDM. In other words, can the CNN serve as a computational model for *affordance-related* responses in the OPA? To address this question, we combined the RSA approach with commonality analysis [32], a variance partitioning technique in which the explained variance

of a multiple regression model is divided into the unique and shared variance contributed by all of its predictors. In this case, multiple regression RSA was used to construct an encoding model of OPA representations. Thus, the OPA was the predictand and the affordance and CNN models were predictors. Our goal was to identify the portion of the shared variance between the affordance RDM and OPA RDM that could be accounted for by the CNN RDM (Fig 3A). This analysis showed that the CNN could explain a substantial portion of the representational similarity between the navigational-affordance model and the OPA. In particular, over half of the explained variance of the navigational-affordance RDM could be accounted for by layer 5 of the CNN (Fig 3B). This suggests that the CNN can serve as a candidate, quantitative model of affordance-related responses in the OPA.

One of the most important aspects of the CNN as a candidate model of affordance-related cortical responses is that it is image computable, meaning that its representations can be calculated for any input image. This makes it possible to test predictions about the internal computations of the model by generating new stimuli and running *in silico* experiments. In the next two sections, we run a series of experiments on the CNN to gain insights into the factors that underlie its predictive accuracy in explaining the representations of the navigational-affordance model and the OPA.

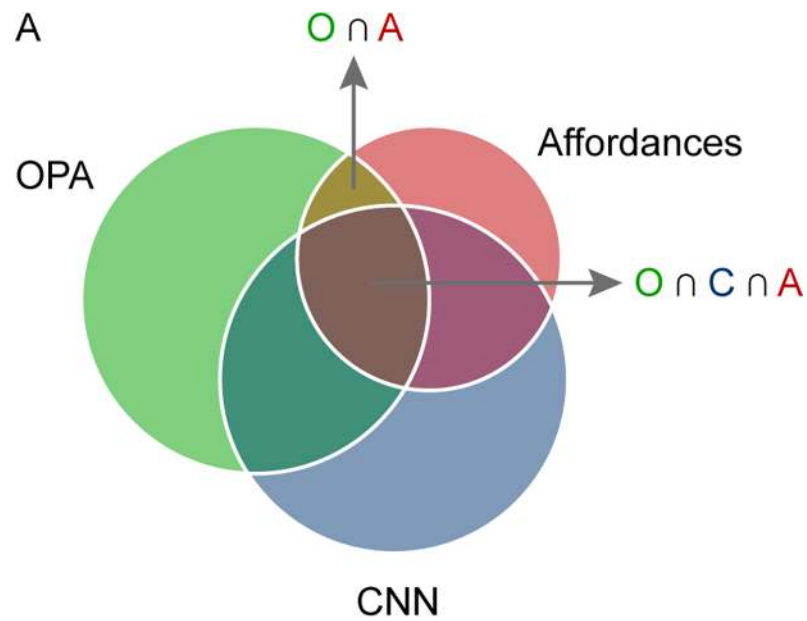
### Low-level image features that underlie the predictive accuracy of the computational model

A fundamental issue for understanding any model of sensory computation is determining the aspects of the sensory stimulus on which it operates. In other words, what sensory inputs drive the responses of the model? To answer this question, we investigated the image features that drive affordance-related responses in the CNN. Specifically, we sought to identify classes of low-level stimulus features that are critical for explaining the representational similarity of the CNN to the navigational-affordance model and the OPA.

We expected that navigational affordances would rely on image features that convey information about the spatial structure of scenes. Our specific hypotheses were that affordance-related representations would be relatively unaffected by color information and would rely heavily on high spatial frequencies and edges at cardinal orientations (i.e., horizontal and vertical). The hypothesis that color information would be unimportant was motivated by our intuition that color is not typically a defining feature of the structural properties of scenes and by a previous finding of ours showing that affordance representations in the OPA are partially tolerant to variations in scene textures and colors [19]. The other two hypotheses were motivated by previous work suggesting that high spatial frequencies and cardinal orientations are especially informative for the perceptual analysis of spatial scenes, and that the PPA and possibly other scene-selective regions are particularly sensitive to these low-level visual features [33–38], but see [39].

To test these hypotheses, we generated new sets of filtered stimuli in which specific visual features were isolated or removed (i.e., color, spatial frequencies, cardinal or oblique edges; Fig 4A and 4B). These filtered stimuli were passed through the CNN, and new RDMs were created for each layer. We used the commonality-analysis technique described in the previous section to quantify the portion of the original explained variance of the CNN that could be accounted for by the filtered stimuli. This procedure was applied to the explained variance of the CNN for predicting both the navigational-affordance RDM and the OPA RDM (Fig 4A). The results for both sets of analyses showed that over half of the explained variance of the CNN could be accounted for when the inputs contained only grayscale information, high-spatial frequencies, or edges at cardinal orientations. In contrast, when input images containing only low-spatial frequencies or oblique edges were used, a much smaller portion of the explained variance was





$$\text{Shared variance} = \frac{(O \cap C \cap A)}{(O \cap C \cap A) + (O \cap A)}$$

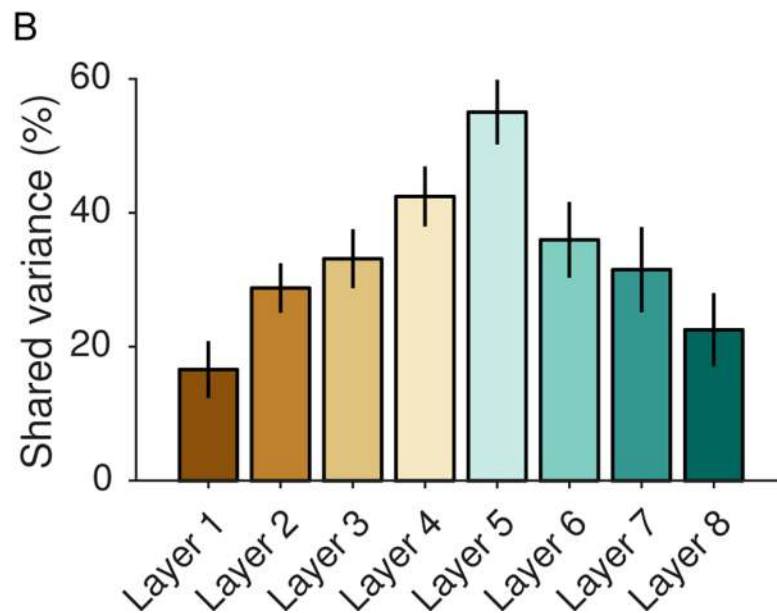


**Fig 3. The CNN accounts for shared variance between OPA responses and the navigational-affordance model.** (A) A variance-partitioning procedure, known as commonality analysis, was used to quantify the portion of the shared variance between the OPA RDM and the navigational-affordance RDM that could be accounted for by the CNN. Commonality analysis partitions the explained variance of a multiple regression model into the unique and shared variance contributed by all of its predictors. In this case, multiple regression RSA was performed with the OPA as the predictand and the affordance and CNN models as predictors. (B) Partitioning the explained variance of the affordance and CNN models showed that over half of the variance explained by the navigational-affordance model in

the OPA could be accounted for by the highest convolutional layer of the CNN (layer 5). Error bars represent bootstrap  $\pm 1$  s.e.m.

<https://doi.org/10.1371/journal.pcbi.1006111.g003>

accounted for. The differences in explained variance across high and low spatial frequencies and across cardinal and oblique orientations were more pronounced for the RSA predictions of the affordance RDM, but a similar pattern was observed for the OPA RDM. We used a

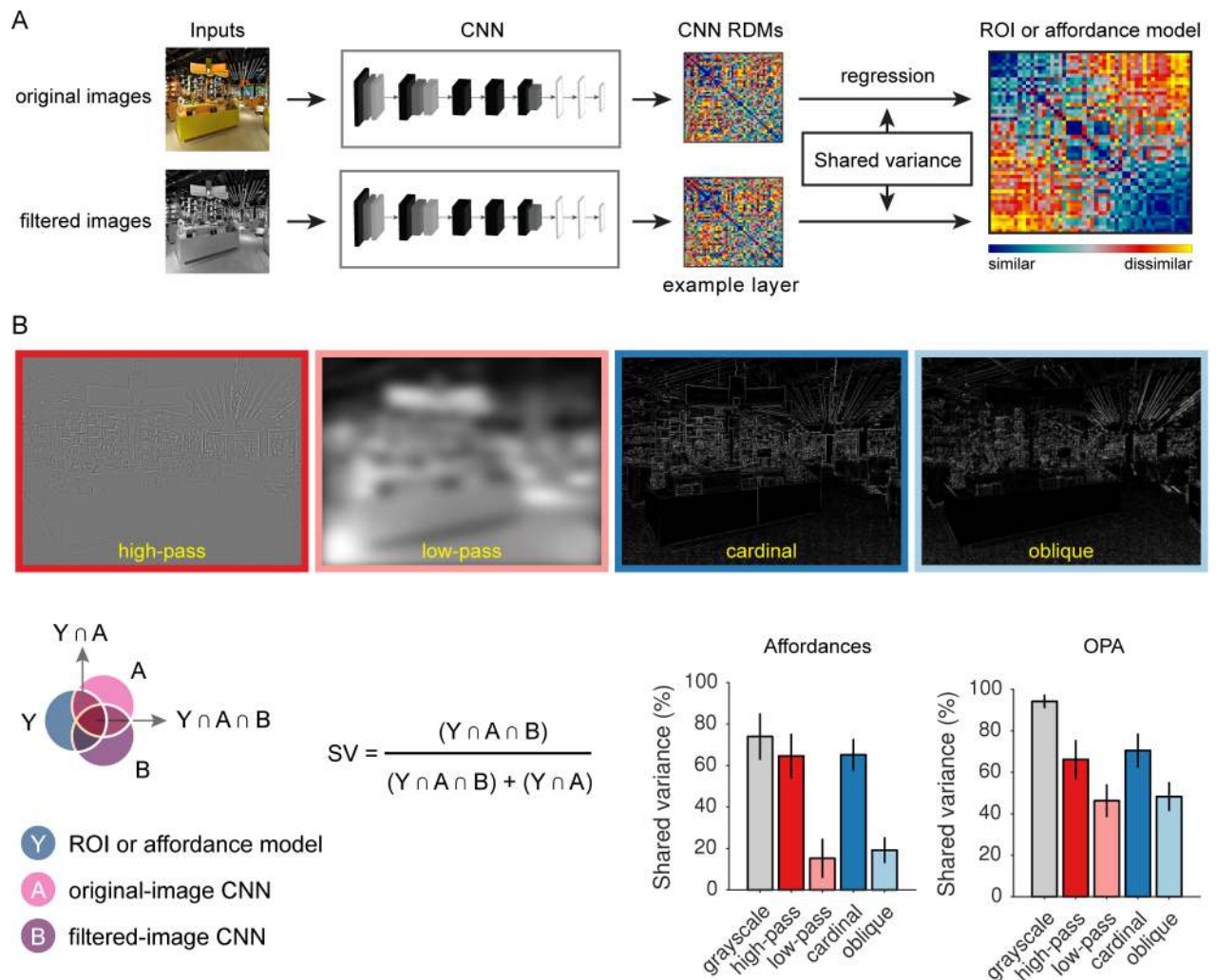


**Fig 4. Analysis of low-level image features that underlie the predictive accuracy of the CNN.** (A) Experiments were run on the CNN to quantify the contribution of specific low-level image features to the representational similarity between the CNN and the OPA and between the CNN and the navigational-affordance model. First, the original stimuli were passed through the CNN, and RDMs were created for each layer. Then the stimuli were filtered to isolate or remove specific visual features. For example, grayscale images were created to remove color information. These filtered stimuli were passed through the CNN, and new RDMs were created for each layer. Multiple-regression RSA was performed using the RDMs for the original and filtered stimuli as predictors. Commonality analysis was applied to this regression model to quantify the portion of the shared variance between the CNN RDM and the OPA RDM or between the CNN RDM and the affordance RDM that could be accounted for by the filtered stimuli. (B) This procedure was used to quantify the contribution of color (grayscale), spatial frequencies (high-pass and low-pass), and edge orientations (cardinal and oblique). The RSA effects of the CNN were driven most strongly by grayscale information at high spatial frequencies and cardinal orientations. Over half of the shared variance between the CNN and the OPA and between the CNN and the affordance model could be accounted for by representations of grayscale images or images containing only high-spatial frequency information or edges at cardinal orientations. In contrast, the contributions of low spatial frequencies and edges at oblique orientations were considerably lower. These differences in high-versus-low spatial frequencies and cardinal-versus-oblique orientations were more pronounced for RSA predictions of the navigational-affordance RDM, but a similar pattern was observed for the OPA RDM. Bars represent means and error bars represent  $\pm 1$  s.e.m. across CNN layers.

<https://doi.org/10.1371/journal.pcbi.1006111.g004>

bootstrap resampling procedure to statistically assess these comparisons. Specifically, we calculated bootstrap 95% confidence intervals for the following contrasts of shared-variance scores: 1) high spatial frequencies minus low spatial frequencies and 2) cardinal orientations minus oblique orientations. These analyses showed that the differences in shared variance for high vs. low spatial frequencies and for cardinal vs. oblique orientations were reliable for both the affordance RDM and the OPA RDM (all  $p < 0.05$ , bootstrap).

Together, these results suggest that visual inputs at high-spatial frequencies and cardinal orientations are important for computing the affordance-related features of the CNN. Furthermore, these computational operations appear to be largely tolerant to the removal of color information. Indeed, it is striking how much explained variance these inputs account for given how much information has been discarded from their corresponding filtered stimulus sets.

### Visual-field biases that underlie the predictive accuracy of the computational model

In addition to examining classes of input features to the CNN, we also sought to understand how inputs from different spatial positions in the image affected the similarity between the CNN and RDMs for the navigational-affordance model and the OPA. Our hypothesis was that these RSA effects would be driven most strongly by inputs from the lower visual field (we use the term “visual field” here because the fMRI subjects were asked to maintain central fixation throughout the experiment). This was motivated by previous findings showing that the OPA has a retinotopic bias for the lower visual field [40, 41] and the intuitive prediction that the navigational affordances of local space rely heavily on features close to the ground plane.

To test this hypothesis, we generated sets of occluded stimuli in which everything except a small horizontal slice of the image was masked (Fig 5). These occluded stimuli were passed through the CNN, and new RDMs were created for each layer. Once again, we used the commonality-analysis technique described above to quantify the portion of the original explained variance of the CNN that could still be accounted for by these occluded stimuli. This procedure was repeated with the un-occluded region slightly shifted on each iteration until the entire vertical extent of the image was sampled. We used this procedure to analyze the explained variance of the CNN for predicting both the navigational-affordance RDM and the OPA RDM (Fig 5). For comparison, we also applied this procedure to RDMs for the other ROIs. These analyses showed that the predictive accuracy of the CNN for both the affordance model and the OPA was driven most strongly by inputs from the lower visual field. Strikingly, as much as 70% of the explained variance of the CNN in the OPA could be accounted for by a small horizontal band of features at the bottom of the image (Fig 5). We created a summary statistic for this visual-field bias by calculating the difference in mean shared variance across the lower and upper halves of the image. A comparison of this summary statistic across all tested RDMs shows that the lower visual field bias was observed for the RSA predictions of the affordance model and the OPA, but not for the other ROIs (Fig 5).

Together, these results demonstrate that information from the lower visual field is critical to the performance of the CNN in predicting the affordance RDM and the OPA RDM. These findings are consistent with previous neuroimaging work on the retinotopic biases of the OPA [40, 41], and they suggest that the cortical computation of affordance-related features reflects a strong bias for inputs from the lower visual field.

### High-level features of the computational model that best account for affordance-related cortical representations

The analyses above examined the stimulus inputs that drive affordance-related computations in the CNN. We next set out to characterize the high-level features that result from these

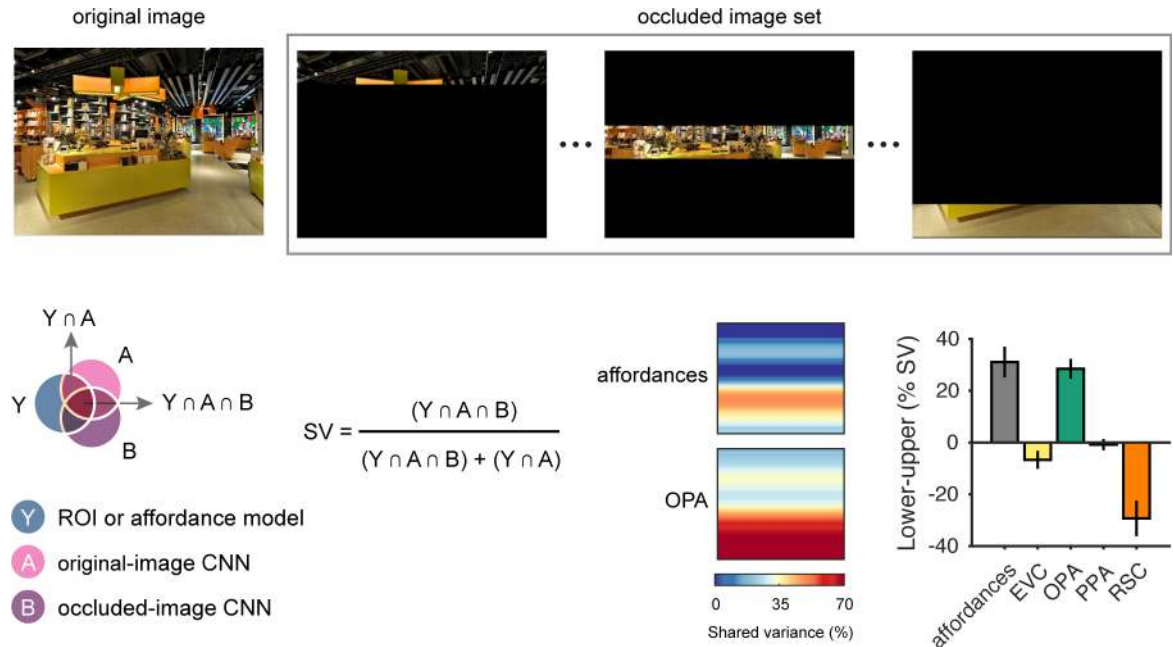


**Fig 5. Visual-field biases in the predictive accuracy of the CNN.** Experiments were run on the CNN to quantify the importance of visual inputs at different positions along the vertical axis of the image. First, the original stimuli were passed through the CNN, and RDMs were created. Then the stimuli were occluded to mask everything outside of a small horizontal slice of the image (top panel). These occluded stimuli were passed through the CNN, and new RDMs were created. Multiple regression RSA was performed using the RDMs for the original and occluded images as predictors. Commonality analysis was applied to this regression model to quantify the portion of the shared variance between the CNN and the OPA or between the CNN and the navigational-affordance model that could be accounted for by the occluded images (bottom left panel). This procedure was repeated with the un-occluded region slightly shifted on each iteration until the entire vertical axis of the image was sampled. Results indicated that the RSA effects of the CNN were driven most strongly by features in the lower half of the image (bottom right panel). This effect was most pronounced for RSA predictions of the OPA RDM, in which ~70% of the explained variance of the CNN could be accounted for by visual information within a small slice of the image from the lower visual field. A summary statistic of this visual-field bias, created by calculating the difference in mean shared variance across the lower and upper halves of the image, showed that a bias for information in the lower visual field was observed for the affordance model and the OPA, but not for EVC, PPA, or RSC. Bars represent means and error bars represent  $\pm 1$  s.e.m. across CNN layers.

<https://doi.org/10.1371/journal.pcbi.1006111.g005>

computations. Specifically, we sought to characterize the internal representations of the CNN that best account for the representations of the OPA and the navigational-affordance model. To do this, we performed a set of visualization analyses to reify the complex visual motifs detected by the internal units of the CNN.

We characterized the feature selectivity of CNN units using a receptive-field mapping procedure (Fig 6A) [42]. The goal was to identify natural image features that drive the internal representations of the CNN. In this procedure, the selectivity of individual CNN units was mapped across each image by iteratively occluding the inputs to the CNN. First, the original, un-occluded image was passed through the CNN. Then a small portion of the image was occluded with a patch of random pixel values (11 pixels by 11 pixels). The occluded image was passed through the CNN, and the discrepancies in unit activations relative to the original image were logged. These discrepancy values were calculated for each unit by taking the difference in magnitude between the activation to the original image and the activation to the occluded image. After iteratively applying this procedure across all spatial positions in the image, a two-dimensional discrepancy map was generated for each unit and each image (Fig 6A). Each discrepancy map indicates the sensitivity of a CNN unit to the visual information across all spatial positions of an image. The spatial distribution of the discrepancy effects reflects the position and extent of a unit's receptive field, and the magnitude of the discrepancy effects reflects the



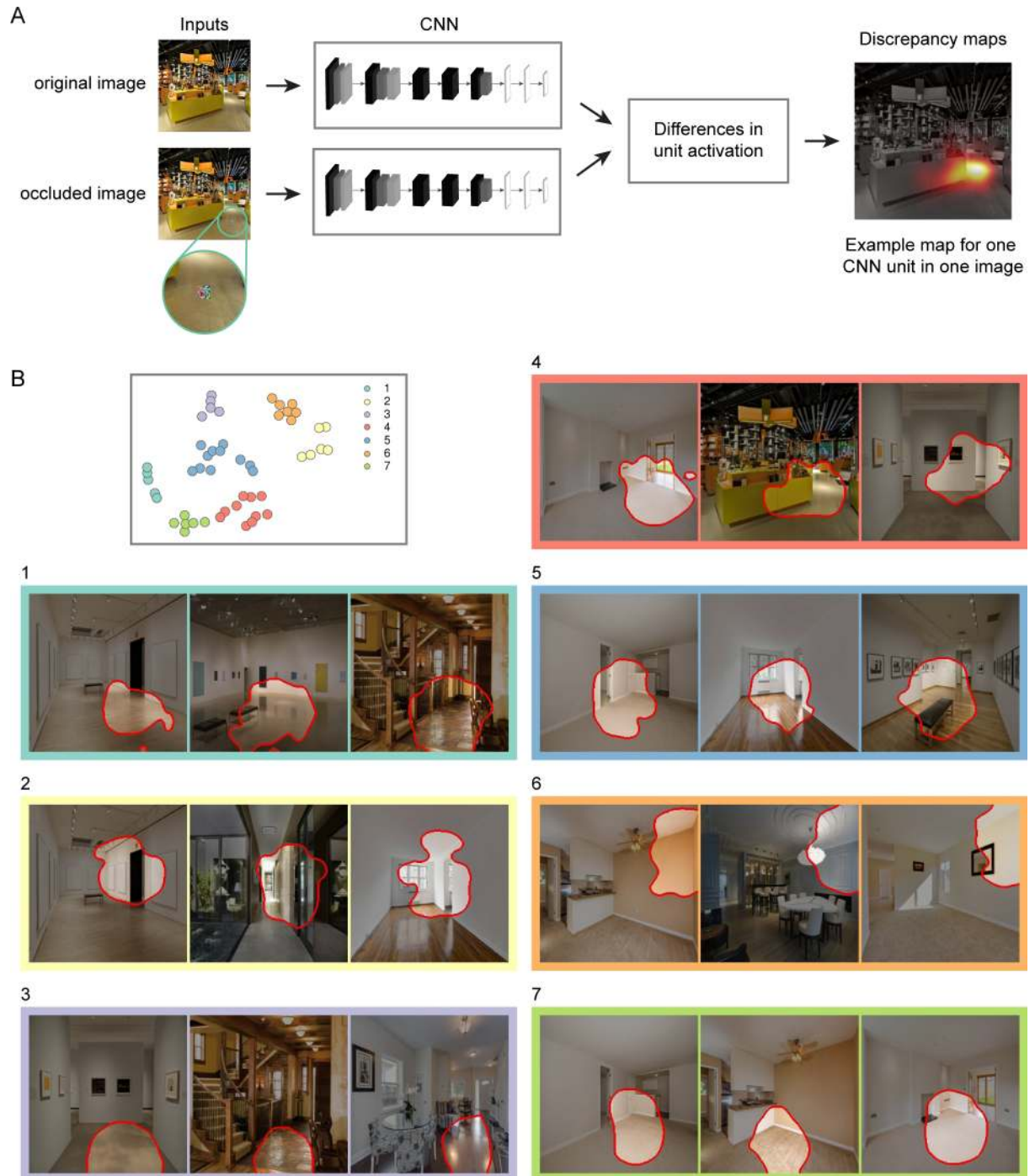


**Fig 6. Receptive-field selectivity of CNN units.** (A) The selectivity of individual CNN units was mapped across each image through an iterative occlusion procedure. First, the original image was passed through the CNN. Then a small portion of the image was occluded with a patch of random pixel values. The occluded image was passed through the CNN, and the discrepancies in unit activations relative to the original image were logged. After iteratively applying this procedure across all spatial positions in the image, a two-dimensional discrepancy map was generated for each CNN unit and each stimulus (far right panel). Each discrepancy map indicates the sensitivity of a CNN unit to the visual information within an image. The two-dimensional position of its peak effect reflects the unit's spatial receptive field, and the magnitude of its peak effect reflects the unit's selectivity for the image features within this receptive field. (B) Receptive-field visualizations were generated for a subset of the units in layer 5 that had strong unit-wise RSA correlations with the OPA and the affordance model. To examine the visual motifs detected by these units, we created a two-dimensional embedding of the units based on the visual similarity of the image features that drove their responses. A clustering algorithm was then used to identify groups of units whose responses reflect similar visual motifs (top left panel). This data-driven procedure identified 7 clusters, which are color-coded and numbered in the two-dimensional embedding. Visualizations are



shown for an example unit from each cluster (the complete set of visualizations can be seen in [S1–S7 Figs](#)). These visualizations were created by identifying the top 3 images with the largest discrepancy values in the receptive-field mapping procedure (i.e., images that were strongly representative of a unit's preferences). A segmentation mask was then applied to each image by thresholding the unit's discrepancy map at 10% of the peak discrepancy value. Segmentations highlight the portion of the image that the unit was sensitive to. Each segmentation is outlined in red, and regions of the image outside of the segmentation are darkened. Among these visualizations, two broad themes were discernable: boundary-defining junctions (e.g., clusters 1, 5, 6, and 7) and large extended surfaces (e.g., cluster 3). The boundary-defining junctions included junctions where two or more large planes meet (e.g., a wall and a floor). Large extended surfaces included uninterrupted portions of floor and wall planes. There were also units that detected features indicative of doorways and other open pathways (e.g., clusters 2 and 4). All of these high-level features appear to be well-suited for mapping out the spatial layout and navigational boundaries in a visual scene.

<https://doi.org/10.1371/journal.pcbi.1006111.g006>

sensitivity of a unit to the underlying image features. We focused our analyses on the units in layer 5, which was the layer with the highest RSA correlation for the both the navigational-affordance model and the OPA. We selected 50 units in this layer based on their unit-wise RSA correlations to the navigational-affordance model and the OPA. These units were highly informative for our effects of interest: an RDM created from just these 50 units showed comparable RSA correlations to those observed when using all units in layer 5 (correlation with affordance RDM:  $r = 0.28$ ; correlation with OPA RDM:  $r = 0.35$ ). We generated receptive-field visualizations for each of these units. These visualizations were created by identifying the top 3 images that generated the largest discrepancy values in the receptive-field mapping procedure (i.e., images that were strongly representative of a unit's preferences). A segmentation mask was then applied to each image by thresholding the unit's discrepancy map at 10% of the peak discrepancy value. Segmentations highlight the portion of the image that the unit was sensitive to. Each segmentation is outlined in red, and regions of the image outside of the segmentation are darkened ([Fig 6B](#)).

We sought to identify prominent trends across this set of receptive-field segmentations. In a simple visual inspection of the segmentations, we detected visual motifs that were common among the units, and the results of an automated clustering procedure highlighted these trends. Using data-driven techniques, we embedded the segmentations into a low-dimensional space and then partitioned them into clusters with similar visual motifs. We used t-distributed stochastic neighbor embedding (t-SNE) to generate a two-dimensional embedding of the units based on the visual similarity of their receptive-field segmentations ([Fig 6B](#)). We then used k-means clustering to identify sets of units with similar embeddings. The number of clusters was set at 7 based on the outcome of a cluster-evaluation procedure. The specific cluster assignments do not necessarily indicate major qualitative distinctions between units. Rather, they provide a data-driven means of reducing the complexity of the results and highlighting the broad themes in the data. These themes can also be seen in the complete set of visualizations plotted in [S1–S7 Figs](#).

These visualizations revealed two broad visual motifs: boundary-defining junctions and large, extended surfaces. Boundary-defining junctions are the regions of an image where two or more extended planes meet (e.g., clusters 1, 5, 6, and 7 in [Fig 6B](#)). These were often the junctions of walls and floors, and less often ceilings. This was the most common visual motif across all segmentations. Large, extended surfaces were uninterrupted portions of floor and wall planes (e.g., cluster 3 in [Fig 6B](#)). There were also units that detected more complex structural features that were often indicative of doorways and other open pathways (e.g., clusters 2 and 4 in [Fig 6B](#)).

A common thread running through all these visualizations is that they appear to reflect high-level scene features that could be reliably used to map out the spatial layout and navigational affordances of the local environment. Boundary-defining junctions and large, extended surfaces provide critical information about the spatial geometry of the local scene, and more fine-grained structural elements, such as doorways and open pathways, are critical to the

navigational layout of a scene. Together, these results suggest a minimal set of high-level visual features that are critical for modeling the navigational affordances of natural images and predicting the affordance-related responses of scene-selective visual cortex.

### Identifying the navigational properties of natural landscapes

Our analyses thus far have focused on a carefully selected set of indoor scenes in which the potential for navigation was clearly delimited by the spatial layout of impassable boundaries and solid open ground. Indeed, the built environments depicted in our stimuli were designed so that humans could readily navigate through them. However, there are many environments in which navigability is determined by a more complex set of perceptual factors. For example, in outdoor scenes navigability can be strongly influenced by the material properties of the ground plane (e.g., grass, water). We wondered whether the components of the CNN that were related to the navigational-affordance properties of our indoor scenes could be used to identify navigational properties in a broader range of images.

To address this question, we examined a set of images depicting natural landscapes, whose navigational properties had been quantified in a previous behavioral study [43]. Specifically, these stimuli included 100 images that could be grouped into categories of low or high navigability based on subjective behavioral assessments. The overall navigability of the images reflected subjects' judgments of how easily they could move through the scene. These navigability assessments were influenced by a wide range of scene features, including the spatial layout of pathways and boundaries, the presence of clutter and obstacles, and the potential for treacherous conditions. There were also low and high categories for 13 other scene properties (Fig 7A). Each scene property was associated with 100 images (50 low and 50 high), and many images were used for multiple scene properties (548 images in total). We sought to determine whether the units from the CNN that were highly informative for identifying the navigational affordances of indoor scenes could also discern the navigational properties in this heterogeneous set of natural landscapes. To do this, we focused on the 50 units selected for the visualization analyses in Fig 6, and we used the responses of these units to classify natural landscapes based on their overall navigability (Fig 7A). We found that not only were these CNN units able to classify navigability across a broad range of outdoor scenes, but they also appeared to be particularly informative for this task relative to the other units in layer 5 (99<sup>th</sup> percentile in a resampling distribution). Furthermore, these units were substantially better at classifying navigability than any other scene property (chi-squared tests for equality of proportions: all  $p < 0.05$ , Bonferroni corrected). These findings suggest that the navigation-related components of the CNN detected in our previous analyses can generalize beyond the domain of built environments to identify the navigability of complex natural landscapes, whose navigational properties reflect a diverse set of high-level perceptual cues.

Example images from the classification analysis of navigability are shown in Fig 7B and 7C. These images were classified based on the responses of the affordance-related CNN units. The correctly classified images span a broad range of semantic categories and have complex spatial and navigational properties (Fig 7B). Spatial layout alone appears to be insufficient for explaining the performance of this classifier. For example, the high-navigability scenes could have either open or closed spatial geometries, and many of the low-navigability scenes have open ground but would be challenging to navigate because of the materials or obstacles that they contain (e.g., water, dense brush). This suggests that the affordance-related components of the CNN are sensitive to scene properties other than coarse-scale spatial layout and could potentially be used to detect a broader set of navigational cues, including textures and material properties. However, textures and materials also appeared to underlie some of the confusions of the

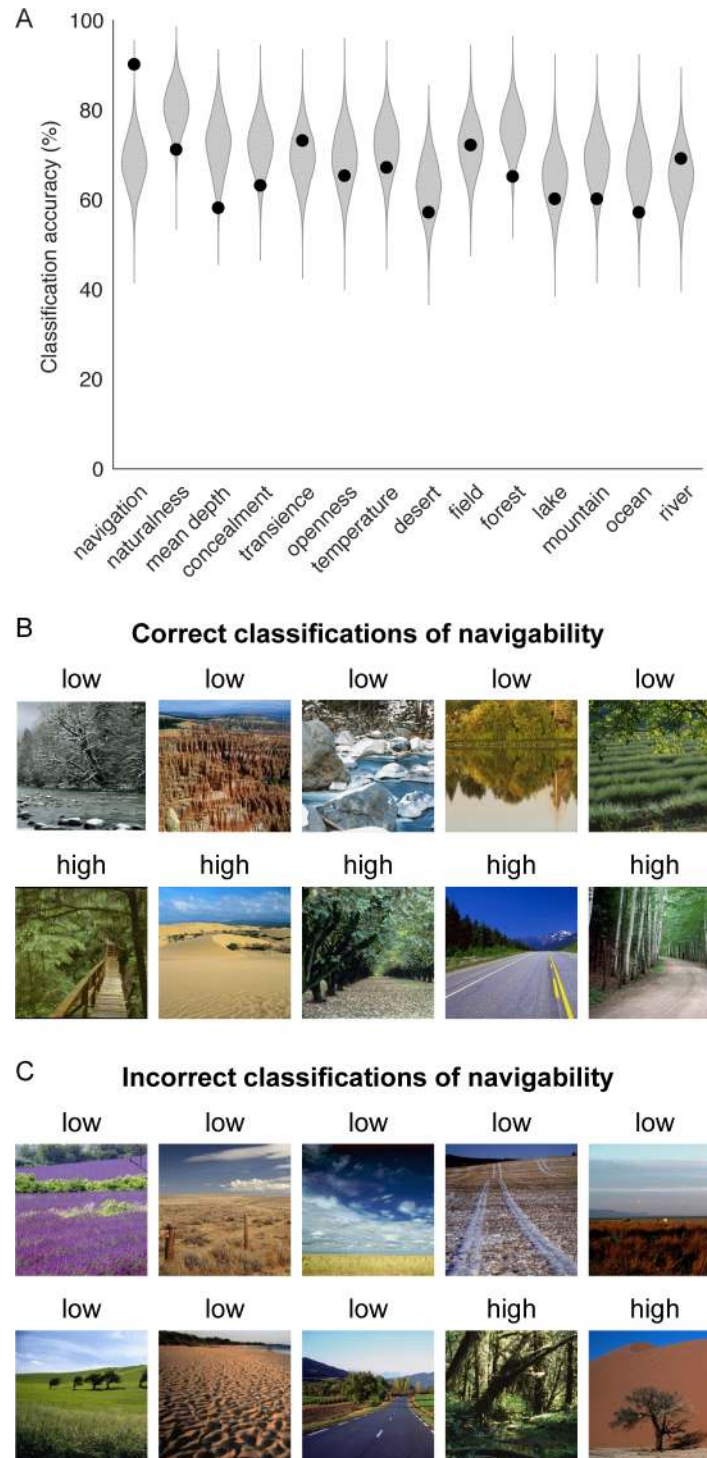


**Fig 7. Classification of navigability in natural landscapes.** (A) Units from layer 5 of the CNN were used to classify navigability and other scene properties in a set of natural outdoor scenes. Classifier performance was examined for a subset of units that were strongly associated with navigational-affordance representation in our previous analyses of indoor scenes. Specifically, a classifier was created from the 50 units in layer 5 that were selected for the visualization analyses in Fig 6. For comparison, a resampling distribution was generated by randomly selecting 50 units from layer 5 over 5,000 iterations and submitting these units to the same classification procedures. Classification accuracy was quantified through leave-one-out cross-validation. For each scene property, the label for a given image was predicted from a linear classifier trained on all other images. This procedure was repeated for each image in turn, and accuracy

was calculated as the percentage of correct classifications across all images. In this plot, the black dots indicate the classification accuracies obtained from the 50 affordance-related CNN units, and the shaded kernel density plots indicate the accuracy distributions obtained from randomly resampled units. Each kernel density distribution was mirrored across the vertical axis, with the area in between shaded gray. These analyses showed that the strongly affordance-related units performed at 90% accuracy when classifying natural landscapes based on navigation (i.e., overall navigability). This accuracy was in the 99th percentile of the resampling distribution, suggesting that these units were particularly informative for identifying scene navigability. Furthermore, these units were more accurate at classifying navigation than any other scene property. (B) Examples of images that were correctly classified into the categories of low or high navigability based on the responses of the affordance-related units. These images illustrate some of the high-level scene features that influenced overall navigability, including spatial layout, textures, and material properties. (C) All images that were misclassified into categories of low or high navigability based on the responses of the affordance-related units. The label above each image is the incorrect label produced by the classifier. Many of the misclassified images contain materials on the ground plane that were uncommon in this stimulus set.

<https://doi.org/10.1371/journal.pcbi.1006111.g007>

classifier (Fig 7C). For example, there were multiple instances of scenes covered in dense natural materials that the classifier labeled as low navigability, even though human observers considered them to be readily navigable (e.g., a field of flowers). These classification errors may reflect the limitations of the CNN units for making fine-grained distinctions between navigable and non-navigable materials. However, the materials and textures in these scenes were relatively uncommon among the stimuli, which suggests that a more important underlying factor may be the limited number of relevant training examples.

Overall, these classification analyses demonstrate that the CNN contains internal representations that can be used to identify the navigational properties of both regularly structured built environments and highly-varied natural landscapes. These representations appear to be sensitive to a diverse set of high-level scene features, including not only spatial layout but also scene textures and materials.

## Discussion

We examined a deep CNN from computer vision for insights into the computations of high-level visual cortex during natural scene perception. Previous work has shown that supervised CNNs, trained for tasks such as image classification, are predictive of sensory responses throughout much of visual cortex, but their internal operations are highly complex and remain poorly understood. Here we developed a set of techniques for relating the internal operations of a CNN to cortical sensory functions. Our approach combines hypothesis-driven *in silico* experiments with statistical tools for quantifying the shared representational content in neural and computational systems.

We applied these techniques to understand the computations that give rise to navigational-affordance representations in the OPA. We found that affordance-related cortical responses could be predicted through a set of purely feedforward computations, involving several stages of nonlinear feature transformations. These computations relied heavily on high-spatial-frequency information at cardinal orientations, and were most strongly driven by inputs from the lower visual field. Following several computational stages, this model gives rise to large, complex features that convey information about the structural layout of a scene. Visualization analyses suggested that the most prominent motifs among these high-level features were the junctions and surfaces of extended planes found on walls, floors, and large objects. We also found that these features could be used to classify the navigability of natural landscapes, suggesting that their utility for navigational perception extends beyond the domain of regularly structured built environments. Together, these results identify a biologically plausible set of feedforward computations that account for a critical function of high-level visual cortex, and they shed light on the stimulus features that drive these computations as well as the internal representations that these computations gives rise to. Below we consider the implications of

these results for our understanding of information processing in scene-selective cortex and for the use of CNNs as a tool for understanding biological systems.

### Information processing in scene-selective cortex

These findings have important implications for developing a computational understanding of scene-selective visual cortex. (Note that we use the term “computational” here in its conventional sense and not in the specific sense defined by David Marr [12]. For readers who are familiar with Marr’s levels of description, our analyses can be viewed as largely addressing the algorithmic level.) To gain an understanding of the algorithms implemented by the visual system we first need candidate quantitative models whose parameters and operations can be interpreted for theoretical insights. One of the primary criteria for evaluating such a model is that it explains a substantial portion of stimulus-driven activity in the brain region of interest. Any model that does not meet this necessary criterion is fundamentally insufficient or incorrect. A major strength of the CNN examined here is that it is highly accurate at predicting cortical responses to the perception of natural scenes. Indeed, the CNN explained as much variance in the responses of the OPA as could be expected for any model, after accounting for the portion of OPA variance that could be attributed to noise. Thus, as in previous studies of high-level object perception, the ability of the CNN to reach the noise ceiling for explained variance during scene perception constitutes a major advance in the quantitative modeling of cortical responses [6, 7].

Another strength of the CNN as a candidate model is that its representations can be computed from arbitrary image inputs. This image computability confers two major benefits. First, the internal representations of the CNN can be investigated across all computational stages and mapped onto a cortical hierarchy, allowing for a complete description of the nonlinear transformations that convert sensory inputs into high-level visual features [11]. Second, image computability allows investigators to submit novel stimulus inputs to the CNN for the purpose of testing hypotheses through *in silico* experiments. Here we took advantage of this image computability to test several hypotheses about which stimulus inputs are critical for computing affordance-related visual features and predicting the responses of the OPA. These analyses demonstrated the importance of inputs from the lower visual field (i.e., the bottom of the image when fixation is at the center), which aligns with previous fMRI studies that used receptive-field mapping to identify a lower-field bias in the OPA [40, 41]. These analyses also demonstrated the importance of several low-level image features that have previously been shown to drive the responses of scene-selective visual cortex, including high-spatial frequencies and contours at cardinal orientations [33–38], but see [39].

We also performed visualization experiments on the internal representations of the CNN to identify potential affordance-related scene features that might be encoded in the population responses of the OPA. Our approach involved data-driven visualizations of the image regions detected by individual CNN units. We focused on the fifth convolutional layer of the CNN and, in particular, on units in this layer that corresponded most strongly to the representations of the OPA and the navigational-affordance model. Among the scene features detected by these units, two broad themes were prominent: boundary-defining junctions and large, extended surfaces. Boundary-defining junctions were contours where two or more large and often orthogonal surfaces were adjoined. These included extended junctions of two surfaces, such as a wall and a floor, and corners where three surfaces come together, such as two walls and a floor. Thus, boundary-defining junctions resembled the basic features that one would use to sketch the spatial layout of a scene.

The idea that such features might be encoded in scene-selective visual cortex accords with previous findings from neuroimaging and electrophysiology. The most directly related



findings come from a series of neuroimaging studies investigating the responses of scene-selective cortex to line drawings of natural images [44, 45]. These line-drawing stimuli convey information about contours and their spatial arrangement, but they lack many of the rich details of natural images, including color, texture, and shading. Nonetheless, these stimuli elicit representations of scene-category information in scene-selective visual cortex. These effects appear to be driven mostly by long contours and their junctions, whose arrangement conveys information about the spatial structure of a scene. This suggests that a substantial portion of the features encoded by scene-selective cortex can be computed using only structure-defining contour information. This aligns with the findings from our visualization analyses, which suggest that large surface junctions are an important component of the information encoded by scene-selective visual cortex. These surface junctions correspond to the long structure-defining contours that would be highlighted in a line drawing. Electrophysiological investigations of scene-selective visual cortex in the macaque brain have also demonstrated the importance of structure-defining contours [46], and even identified cells that exhibited selectivity for the surface junctions in rooms, which appears to be remarkably similar to the selectivity for boundary-defining junctions identified here. Our findings are also broadly consistent with previous behavioral studies demonstrating that contours and contour junctions in 2D images are highly informative about the arrangement of surfaces in 3D space [47]. In particular, contour junctions convey information about 3D structure that is largely invariant to changes in viewpoint, making them exceptionally useful for inferring spatial structure [47].

In addition to boundary-defining junctions, we also observed selectivity for large extended surfaces. One recent study has suggested that the responses of scene-selective visual cortex can be well predicted from the depth and orientation of large surfaces in natural scenes [48]. This appears to be consistent with our finding, but other possible roles for the surface-preferring units in our study include texture identification and the use of texture gradients as 3D orientation cues [49, 50]. Overall, this pattern of selectivity for large surfaces and the junctions between them is consistent with an information-processing mechanism for representing the spatial structure of the local visual environment [12]. However, the findings from our analysis of natural landscapes suggest that the affordance-related components of the CNN are additionally sensitive to other navigational cues, such as the textures and materials in outdoor scenes (e.g., water, grass). Thus, these affordance-related units may encode multiple aspects of the space-defining surfaces in a scene, including their structure and their material properties.

These computational findings have implications for interpreting previous neuroimaging studies of scene-selective cortex. It has been argued that the apparent category selectivity of scene regions can be explained more parsimoniously in terms of preferences for low-level image features, such as high spatial frequencies [33–37], but see [39]. However, the analyses presented here suggest an alternative interpretation, namely that scene-selective visual regions encode complex features that convey information about high-level scene properties, such as navigational layout and category membership, but that the computations that give rise to these features rely heavily on specific sets of low-level inputs [38, 51]. This account characterizes the function of scene-selective visual cortex within the context of a computational system, and it demonstrates how a region within this system could exhibit response preferences for the low-level features that drive its upstream inputs. Thus, by examining a candidate computational model, we identified a potential mechanism through which neuroimaging studies could produce seemingly contradictory findings on the feature selectivity of scene-selective cortex. More broadly, these analyses demonstrate the importance of building explicit computational models to evaluate functional theories of high-level visual cortex. Doing so allows investigators to interpret cortical processes in terms of their functional significance to systems-level computations rather than region-specific representational models.

## Using deep CNNs to obtain insights into biological vision

The analyses and techniques presented here are broadly relevant to research on the functions of visual cortex. A major goal of visual neuroscience is to understand the information-processing mechanisms that visual cortex carries out [12]. Progress toward this goal can be assessed by how well investigators are able to implement these mechanisms *de novo* using models that reflect a compact set of theoretical principles. To this end, investigators require models that are constructed from mathematical algorithms, to allow for implementations in any suitable computational hardware, and whose internal operations are theoretically interpretable, in the sense that one can provide summary descriptions of the functions they carry out and the theoretical principles they embody. A long line of work in visual neuroscience has attempted to understand the information-processing mechanisms of visual cortex by hand-engineering computational models based on *a priori* theoretical principles [29, 30, 52]. Although this approach has been fruitful in characterizing the earliest stages of visual processing, it has not proved effective for explaining the functions of mid-to-high-level visual cortex, where the complexity of the operations and the number of possible features grows exponentially [11]. Recent advances in the development of deep CNNs trained for computer vision have incidentally yielded quantitative models that are remarkably accurate at predicting functional activity throughout much of the visual system [5–11]. However, from a theoretical perspective, these highly complex models have remained largely opaque, and little is known about what aspects of these models might be relevant for understanding the information processes of biological vision.

Here we developed an approach for probing the internal operations of a CNN for insights into cortical computation. Our approach uses RSA in the context of multiple linear regression to evaluate similarities between computational, theoretical, and neural systems. A major benefit of RSA is that it evaluates the information in these systems through summary representations in RDMs, which avoids the many difficulties of identifying mappings between the individual units of high-dimensional systems [28]. We evaluated these multiple linear regressions using a variance-partitioning procedure that allowed us to quantify the degree to which representational models explained shared or unique components of the information content in a cortical region. These statistical methods were combined with techniques for running *in silico* experiments to test theoretically motivated hypotheses about information processing in the CNN and its relationship to the functions of visual cortex. Although we applied these techniques to an exploration of affordance coding in visual scenes, they are broadly applicable and could be used to examine any cortical region or image-computable model. They demonstrate a general approach for exploring how the computations of a CNN relate to the information-processing algorithms of biological vision.

It is worth noting, however, that there are important limitations in using deep neural networks for insights into neurobiological processes. One of the critical limiting factors of the analyses described here is our reliance on a pre-trained computational model. Deep CNNs have large numbers of parameters, which are typically fit through supervised learning using millions of labeled stimuli. Given the cost of manually labeling this number of stimuli and the far smaller number of stimuli used in a typical neuroscience experiment, it is not feasible to train deep neural networks that are customized for the perceptual processes of interest in every new experiment. Fortunately, neuroscientists can take advantage of the fact that deep neural networks trained for real-world tasks using large, naturalistic stimulus sets appear to learn a set of general-purpose representations that often transfer well to other tasks [25, 53, 54]. Furthermore, the objective functions that these CNNs were trained for all relate to computer-vision goals (e.g., object or scene classification), and, yet, their internal representations exhibit

remarkable similarities to those at multiple levels of visual cortex [5–11]. This means that investigators can examine existing pre-trained models for their potential relevance to a cortical sensory process, even if the models were not explicitly trained to implement that process. However, in the analysis of pre-trained models, the architecture, activation function, and other design factors are constrained, and, thus, the results of these analyses cannot be easily compared with alternative algorithmic implementations. An important direction for future work will be the use of multiple models to compare specific architectural and design factors with neural processes, such as the number of model layers, the directions and patterns of connectivity between neurons, the kinds of non-linear operations that the neurons implement, and so on. Nonetheless, we still have much to learn about the information processes of existing CNNs and how they relate to cortical sensory functions, and there is fruitful work to be done in developing techniques that leverage these models for theoretical insights.

Another limitation of this work is that many computer-vision models, and most visual neuroscience experiments, are restricted to simple perceptual tasks using static images. This ignores many important aspects of natural vision that any comprehensive computational model will ultimately need to account for, including attention, motion, temporal dependencies, and the role of memory. Our findings are also limited by the noise ceiling of our neural data. Although the CNN explained as much variance in the OPA as could be expected for any model, there still remains a large portion of variance that can be attributed to noise. This noise arises from multiple factors, including inter-subject variability, variability in cortical responses across stimulus repetitions, the limited resolution of fMRI data, signal contamination from experimental instruments or physiological processes, and irreducible stochasticity in neural activity. Improving the noise ceiling in fMRI studies of high-level visual cortex will be an important goal for future work. Several of these noise-related factors could potentially be mitigated through the use of larger and more naturalistic stimulus sets or through improved data pre-processing procedures. Others, such as inter-subject and inter-trial variability may have identifiable underlying causes that are important for understanding the functional algorithms of high-level visual cortex [55, 56].

In addition to the experimental approaches used here, there are other important avenues of investigation for relating the computations of neural networks to the visual system. For example, CNNs could be used to generate new stimuli that are optimized for testing specific computational hypotheses [17], and then fMRI data could be collected to examine the role of these computations in visual cortex. Another useful approach would be to run *in silico* lesion studies on CNNs to understand the role of specific units within a computational system. Finally, an important direction for future work will be to use the conclusions of experiments on CNNs to build simpler models that embody specific computational principles and allow for detailed investigations of the necessary and sufficient components of information processing in vision.

## Conclusion

An important goal of neuroscience is to understand the computational operations of biological vision. In this work, we utilized recent advances in computer vision to identify an image-computable, quantitative model of navigational-affordance coding in scene-selective visual cortex. By running experiments on this computational model, we characterized the stimulus inputs that drive its internal representations, and we revealed the complex, high-level scene features that its computations give rise to. Together, this work suggests a computational mechanism through which visual cortex might encode the spatial structure of the local navigational environment, and it demonstrates a set of broadly applicable techniques that can be used to relate the internal operations of deep neural networks with the computational processes of the brain.

## Methods

### Ethics statement

We analyzed human fMRI data that were described in a previous publication, which includes a complete description of IRB approval and subject consent [19].

### Representational similarity analysis

We used RSA to characterize the navigational-affordance information contained in multivoxel fMRI-activation patterns and multiunit CNN-activity patterns.

For the fMRI data, we extracted activation patterns from a set of functionally defined ROIs for each of the 50 images in the stimulus set, using the procedures described in our previous report [19]. Briefly, 16 subjects viewed 50 images of indoor scenes presented for 1.5 s each in 10 scan runs, and performed a category-detection task. Subjects were asked to fixate on a central cross that remained on the screen at all times and press a button if the scene they were viewing was a bathroom. A general linear model was used to extract voxelwise responses to each image in each scan run. ROIs were based on a standard set of functional localizers collected in separate scan runs, and they were defined using an automated procedure with group-based anatomical constraints [19, 57, 58].

For each subject, the responses of each voxel in an ROI were z-scored across images within each run and then averaged across runs. We then applied a second normalization procedure in which the response patterns for each image were z-scored across voxels. Subject-level RDMs were created by calculating the squared Euclidean distances between these normalized response patterns for all pairwise comparisons of images. The squared Euclidean distance metric was used (here and for the other RDMs described below) because several of our analyses involved multiple linear regression for assessing representational similarity. In this framework, the distances from one RDM are modeled as linear combinations of the distances from a set of predictor RDMs. This requires the use of a distance metric that sums linearly [6, 59]. Squared Euclidean distances sum linearly according to the Pythagorean theorem, and when the representational patterns are normalized (i.e., z-scored across units), these distances are linearly proportional to Pearson correlation distances, which we used in our previous analyses of these data [19]. We then constructed group-level neural RDMs for each ROI by taking the mean across all subject-level RDMs. The use of group-level RDMs allowed us to apply the same statistical procedures for assessing all comparisons of RDMs (i.e., fMRI RDMs, navigational-affordance RDM, and CNN RDMs). Furthermore, the use of group-level RDMs, which are averaged across subjects, has the benefit of increasing signal-to-noise and improving model fits for the RSA comparisons.

To construct RDMs for each layer of the CNN, we first ran the experimental stimuli through a pre-trained CNN that can be downloaded here: [http://places.csail.mit.edu/model/placesCNN\\_upgraded.tar.gz](http://places.csail.mit.edu/model/placesCNN_upgraded.tar.gz). We recorded the activations from the final outputs of all linear-nonlinear operations within each layer of the CNN. All layers, with the exception of layer 8, contain thousands of units. We found that the RSA correlations between the layers of the CNN and the ROIs were improved when the dimensionality of the CNN representations was reduced through principal component analysis (PCA). This likely reflects the fact that all CNN units were weighted equally in our calculations of representational distances, even though many of the units had low variance across our stimuli. PCA reduces the number of representational dimensions and focuses on the components of the data that account for the largest variance. We therefore set the dimensionality of the CNN representations to 45 principal components (PCs) for each layer. Our findings were not contingent

on the specific number of PCs retained; we observed similar results across the range from 30 to 49 PCs. We z-scored the CNN activations across PCs for each image and calculated squared Euclidean distances for all pairwise comparisons of images.

The neural and CNN RDMs were compared with an RDM constructed from the representations of a navigational-affordance model. To construct this model, we calculated representational patterns that reflected the navigability of each scene along a set of angles radiating from the bottom center of the image (Fig 1). These navigability data were obtained in a norming study in which an independent group of raters, who did not participate in the fMRI experiment, indicated the paths that they would take to walk through each scene (Fig 1B) [19]. In our previous report, we combined these navigational data with a set of idealized tuning curves that reduced the dimensionality of the data to a small set of hypothesized encoding channels (i.e., paths to the left, center, and right). Here, however, we used a different approach in which we simply smoothed the navigability data over the 180 degrees of angular bins using an automated and robust smoothing method [60]. This smoothing procedure was implemented using publicly available software from the MATLAB file exchange: <https://www.mathworks.com/matlabcentral/fileexchange/25634-fast-n-easy-smoothing?focused=6600598&tab=function>. We then z-scored these smoothed data across the angular bins for each image and calculated squared Euclidean distances for all pairwise comparisons of images.

For standard RSA comparisons of two RDMs, we calculated representational similarity using Spearman correlations. The Spearman-correlation procedure assesses whether two models exhibit similar rank orders of representational distances, which allows for the possibility of a nonlinear relationship between the pairwise distances of two RDMs. Nonetheless, we observed similar results using Pearson correlations or linear regressions, and thus our RSA findings were not contingent on the use of a non-parametric statistical test. Bootstrap standard errors of these correlations were calculated over 5000 iterations in which the rows and columns of the RDMs were randomly resampled. This is effectively a resampling of the stimulus labels in the RDM. Resampling was performed without replacement by subsampling 90% of the rows and columns of the RDMs. We did not use resampling with replacement because it would involve elements of the RDM diagonals (i.e., comparisons of stimuli to themselves) that were not used when calculating the RSA correlations [61]. All bootstrap resampling procedures were performed in this manner. Statistical significance was assessed through a permutation test in which the rows and columns of one of the RDMs were randomly permuted and a correlation coefficient was calculated over 5000 iterations. P-values were calculated from this permutation distribution for a one-tailed test using the following formula:

$$p \text{ value} = \frac{\sum(R_{perm} \geq R_{test}) + 1}{N + 1}$$

where  $R_{perm}$  refers to the correlation coefficients from the permutation distribution and  $R_{test}$  refers to the correlation coefficient for the original data. All p-values were Bonferroni-corrected for the number of comparisons performed (i.e., the number of ROIs in Fig 1 and the number of CNN layers in Fig 2).

We calculated the noise ceiling for RSA correlations in the OPA as the mean correlation of each subject-level OPA RDM to the overall group-level OPA RDM, a measure that reflects the inherent noise in the fMRI data [62]. According to this metric, the best-fitting model for an ROI should explain as much variance as the average subject.



### Commonality analysis

Several analyses involved the use of multiple linear regression and a variance-partitioning procedure to quantify the overlap of explained variance for two predictor RDMs. The multiple linear regression models included two regressors for the predictor RDMs and a third regressor for the constant term. These regressors were used to explain variance in a third RDM, which served as the dependent variable. Thus, the data points for the dependent and independent variables were the pairwise distance measurements of the RDMs. The models were fit using ordinary least squares regression. We quantified the overlap of explained variance for the two predictor RDMs using a procedure known as commonality analysis [32]. This procedure partitions the explained variance of the regression model into the shared and unique components contributed by all regressors. We used this analysis to determine the degree to which the explained variance of one regressor (e.g., the affordance RDM) was shared with a second regressor (e.g., the CNN RDM). We refer to this quantity as shared variance, and we calculated it using the following formula:

$$SV = 100 * \frac{\gamma_{12}}{\gamma_{12} + \gamma_1}$$

where  $SV$  is the percentage of the explained variance for regressor  $X_1$  that is in common with regressor  $X_2$  (see also Fig 3A). The other variables in this equation refer to components of the overall explained variance ( $R^2_{12}$ ):

$\gamma_1$  = unique contribution of  $X_1$  to  $R^2_{12}$

$\gamma_{12}$  = common contribution of  $X_1$  and  $X_2$  to  $R^2_{12}$

These values are calculated as follows:

$$\gamma_1 = R^2_{12} - R^2_2$$

$$\gamma_{12} = R^2_1 + R^2_2 - R^2_{12}$$

where  $R^2_{12}$  is the explained variance of a regression model with both  $X_1$  and  $X_2$ ,  $R^2_1$  is the explained variance of a model with only  $X_1$ , and  $R^2_2$  is the explained variance of a model with only  $X_2$ .

Bootstrap standard errors of this shared-variance metric were calculated over 5000 iterations in which the rows and columns of the RDMs were randomly resampled and the variance-partitioning procedure was applied to the resampled RDMs.

### Analyses of low-level stimulus inputs

We quantified the contribution of specific low-level image features to the RSA effects of the CNN. To do this, we generated new sets of filtered stimuli in which specific visual features or portions of the image were isolated or removed (e.g., color, spatial frequencies, edges at cardinal or oblique orientations, lower or upper portions of the image; Figs 4 and 5). These filtered stimuli were passed through the CNN, and new RDMs were created for each layer. We used the commonality-analysis technique described above to quantify the portion of the original explained variance of the CNN that could be accounted for by the filtered stimuli. This procedure was applied to the explained variance of the CNN for predicting both the navigational-affordance RDM and the OPA RDM.

We performed five different stimulus transformations to examine specific classes of image features. The first was a simple transformation of the images from color to grayscale that allowed us to assess the importance of color information. The others reflect two broad categories of low-level image properties: spatial frequencies and contour orientations. To examine

the role of spatial frequencies, we created one set of stimuli in which low spatial frequencies were removed from the images (high-pass) and another set in which high spatial frequencies were removed (low-pass). These were created by first converting the images to grayscale, performing a Fourier transform, filtering out a subset of frequencies, and then reconstructing the grayscale images from the filtered Fourier transforms. For the high-pass images, the Fourier spectrum was filtered using a Gaussian filter with a standard deviation set at 0.1 cycles per pixel. A similar approach was used for the low-pass images, with the standard deviation of the Gaussian filter set at 0.0075 cycles per pixel. To examine the role of contour orientations, we created one set of filtered stimuli in which edges at cardinal orientations were emphasized (cardinal) and another set in which edges at oblique orientations were emphasized (oblique). These were created by first converting the images to grayscale and then performing a convolution to extract image contours at cardinal orientations (0 and 90 degrees) or oblique orientations (45 and 135 degrees). The convolution kernels spanned 3 pixels by 3 pixels and are depicted in [S8 Fig](#). Convolutions were performed separately for the two orientations in each set (e.g., 0 and 90 degrees) and a combined output was created by squaring and summing these convolutions and then taking the square root of their sum.

We statistically assessed differences in shared variance across sets of filtered images by calculating confidence intervals on their difference scores. We did this for the following subsets: 1) high-pass minus low-pass and 2) cardinal minus oblique. To do so, we calculated a bootstrap distribution of the difference in shared variance values across each image set over 5000 iterations in which the rows and columns of the RDMs were randomly resampled. From this distribution, we computed the value of the lower 95<sup>th</sup> percentile for a one-tailed test to determine if the 95% confidence interval was above zero.

We also performed analyses to examine the importance of visual inputs at different positions along the vertical axis of the image. To do this, we generated occluded versions of the stimuli in which everything outside of a small horizontal slice of the image was masked. The exposed slice of the image spanned 41 pixels in height, which was 18% of the overall image height. We used commonality analysis to quantify the portion of the original explained variance of the CNN that could be accounted for by the occluded stimuli. This procedure was repeated with the un-occluded region shifted by a stride of 5 pixels on each iteration until the entire vertical axis of the image was sampled. We generated heat maps of these results by assigning shared variance values to the pixels in each horizontal slice and then averaging the values across overlapping slices.

### Visualizations of high-level feature selectivity

We used a receptive-field mapping procedure in combination with a set of data-driven visualization techniques to gain insights into the complex feature selectivity of units within the CNN. The receptive-field mapping and image-segmentation procedures were based on previously published methods [42]. We mapped the selectivity of individual CNN units across each image by iteratively occluding the inputs to the CNN. First, the original image was passed through the CNN. Then a small portion of the image was occluded with a patch of random pixel values of size 11 pixels by 11 pixels, as in [42]. The occluded image was passed through the CNN, and discrepancies in unit activations relative to the original image were logged. These discrepancies were calculated as the absolute value of the difference in activation, which is consistent with the procedure used by Zhou and colleagues [42] (personal communication with Bolei Zhou). On each iteration, the position of the occluding patch was shifted by a stride of 3 pixels. After iteratively applying this procedure across all spatial positions in the image, a two-dimensional discrepancy map was generated for each unit and each image ([Fig 6A](#)). Each discrepancy

map indicates the sensitivity of a CNN unit to the visual information across all spatial positions of an image. The spatial distribution of the discrepancy effects reflects the position and extent of a unit's receptive field, and the magnitude of the discrepancy effects reflects the sensitivity of a unit to the underlying image features.

We generated image segmentations to visualize the scene features that individual CNN units were most sensitive to (Fig 6B). We first smoothed the discrepancy maps by convolving them with a local averaging filter of 20 pixels by 20 pixels. For each unit, we then selected the 3 stimulus images that generated the largest discrepancy values at any spatial location in the image. We segmented these discrepancy maps by identifying pixels with a discrepancy value equal to at least 10% of the peak discrepancy across all pixels. We generated these visualizations for 50 units in layer 5. These units were chosen based on their unit-wise RSA correlations to the affordance RDM and the OPA RDM (we chose the units with the highest mean correlation to these two RDMs).

We then used t-SNE and k-means clustering to generate a summary visualization and to identify common themes among the scene features that were highlighted by these segmentations [63]. Our goal was to cluster the image segmentations based on the similarity of their high-level scene content. We first created image patches of 81 pixels by 81 pixels centered on the peak discrepancy value for the top 3 images for each unit. We ran these image patches through the CNN and logged the responses in layer 5. These responses were then averaged across the top 3 images for each unit, and t-SNE was used to generate a two-dimensional embedding of all 50 units based on the similarity of their mean response vectors from layer 5. We assigned the units in this embedding to clusters with similar scene features (Figs 6B and S1–S7). Clusters were identified in a data-driven manner through k-means clustering, with the number of clusters chosen (within the range of 1 to 10 clusters) using the silhouette criterion in the MATLAB function `evalclusters`.

### Analysis of CNN responses to properties of natural landscapes

We sought to determine whether the affordance-related components of the CNN identified in our previous analyses of indoor scenes could also be used to identify the navigational properties in a set of highly varied outdoor environments. To do this, we examined the classification of navigability in natural landscapes using a stimulus set from a previous study [43]. These stimuli are described in detail elsewhere [43, 64]. Here we summarize their key properties. All stimuli depict outdoor environments, and they were sampled from a diverse set of semantic categories. They were selected based on behavioral data to represent the poles (i.e., low and high) of 14 high-level scene properties, which included global properties, such as navigability, and semantic categories, such as forest. To create these stimulus groups, a large set of images were ranked according to their representativeness for each scene property, based on the subjective assessments of human observers. Images were selected from the lower and upper ranks of representativeness to create binary classes of “low” and “high” ( $n = 50$  images in each class). There were 548 images in total, and many were used across multiple scene properties.

We examined how well these scene properties could be classified from the responses of the CNN. Our analyses focused on the responses in layer 5, which was the layer that showed the strongest effects for navigational-affordance representations in our previous analyses. To begin, we evaluated the classification accuracies obtained when using the responses of all units in layer 5. For this analysis, we used a simple minimum-distance classifier, which avoided the challenges of fitting classifier parameters to a data set in which the number of feature dimensions is much larger than the number of stimuli. All images were run through the CNN, and the activations of layer 5 were recorded. For each scene property, we constructed an RDM for

its 100 associated images. The unit activations were first z-scored across images and then z-scored across units. RDMs were created by calculating the pairwise Euclidean distances between images based on these unit activations. For each scene property, images were classified into categories of “low” or “high” based on their mean pairwise distance to all other images in those categories. For example, to classify an image in the navigation set, we calculated its mean pairwise distances to all low-navigability images and to all high-navigability images (excluding the comparison of the image to itself). The image was then classified into the category with the smallest mean pairwise distance. Using this approach, navigability was classified at an accuracy of 86%, and all other scene properties were classified at an accuracy of 86% or higher. Thus, the representations of layer 5 appear to be informative for a broad range of high-level scene properties, including the navigability of natural landscapes.

We next examined a small subset of units in layer 5 that we found to be particularly informative in our previous analyses. Specifically, we examined the 50 units that were previously selected for the visualization analyses in Fig 6. For each scene property, we quantified the classification accuracy obtained when passing the responses of these units to a linear discriminant analysis in a leave-one-out cross-validation design. In this procedure, a single image was held out and a linear discriminant classifier was fit to the other 99 images. This classifier was then used to generate a prediction for the held-out image (i.e., low or high), and the procedure was repeated for each image in turn. Accuracy was calculated as the percentage of correct classifications across all images. For comparison, we also computed the classification accuracies obtained from randomly selected subsets of units. Specifically, we performed an iterative resampling procedure in which 50 units were randomly selected from layer 5 (without excluding our original 50 units) and then submitted to the same leave-one-out classification analyses described above. This procedure was repeated 5,000 times for each scene property. The resulting accuracy distributions were visualized using kernel density estimation, as implemented in the MATLAB function `ksdensity` (Fig 7A). For the classification of navigability, we observed only a single instance of a resampled accuracy score that exceeded the performance of our original 50 units. Thus, the classifier performance of the affordance-related units was in the 99<sup>th</sup> percentile of this resampling distribution. For all other scene properties, the classification accuracy of the affordance-related units was no higher than the 69<sup>th</sup> percentile.

## Supporting information

**S1 Fig. Receptive-field visualizations for cluster 1.**

(PDF)

**S2 Fig. Receptive-field visualizations for cluster 2.**

(PDF)

**S3 Fig. Receptive-field visualizations for cluster 3.**

(PDF)

**S4 Fig. Receptive-field visualizations for cluster 4.**

(PDF)

**S5 Fig. Receptive-field visualizations for cluster 5.**

(PDF)

**S6 Fig. Receptive-field visualizations for cluster 6.**

(PDF)



**S7 Fig. Receptive-field visualizations for cluster 7.**  
(PDF)

**S8 Fig. Convolution kernels for extracting lines at cardinal and oblique orientations.** Each kernel spans 3 pixels by 3 pixels. (A) Kernels used to extract lines at cardinal orientations (0 and 90 degrees). (B) Kernels used to extract lines at oblique orientations (45 and 135 degrees).  
(PDF)

## Acknowledgments

We thank Michelle R. Greene and Aude Oliva for making their natural-landscape stimuli and associated data publicly available.

## Author Contributions

**Conceptualization:** Michael F. Bonner, Russell A. Epstein.

**Data curation:** Michael F. Bonner.

**Formal analysis:** Michael F. Bonner.

**Funding acquisition:** Russell A. Epstein.

**Investigation:** Michael F. Bonner.

**Methodology:** Michael F. Bonner.

**Software:** Michael F. Bonner.

**Visualization:** Michael F. Bonner.

**Writing – original draft:** Michael F. Bonner, Russell A. Epstein.

**Writing – review & editing:** Michael F. Bonner, Russell A. Epstein.

## References

1. LeCun Y, Bengio Y, Hinton G. Deep learning. *Nature*. 2015; 521(7553):436–44. <https://doi.org/10.1038/nature14539> PMID: 26017442
2. Krizhevsky A, Sutskever I, Hinton GE. Imagenet classification with deep convolutional neural networks. *Advances in neural information processing systems* 2012. p. 1097–105.
3. Zhou B, Lapedriza A, Xiao J, Torralba A, Oliva A. Learning deep features for scene recognition using places database. *Advances in neural information processing systems* 2014. p. 487–95.
4. Rawat W, Wang Z. Deep convolutional neural networks for image classification: a comprehensive review. *Neural Comput*. 2017. Epub June 09, 2017. [https://doi.org/10.1162/NECO\\_a\\_00990](https://doi.org/10.1162/NECO_a_00990) PMID: 28599112.
5. Agrawal P, Stansbury D, Malik J, Gallant JL. Pixels to voxels: modeling visual representation in the human brain. *arXiv preprint arXiv:14075104*. 2014.
6. Khaligh-Razavi S-M, Kriegeskorte N. Deep Supervised, But Not Unsupervised, Models May Explain IT Cortical Representation. *PLoS Computational Biology*. 2014; 10(11):e1003915. <https://doi.org/10.1371/journal.pcbi.1003915> PMID: 25375136
7. Yamins DLK, Hong H, Cadieu CF, Solomon EA, Seibert D, DiCarlo JJ. Performance-optimized hierarchical models predict neural responses in higher visual cortex. *Proceedings of the National Academy of Sciences*. 2014; 111(23):8619–24. <https://doi.org/10.1073/pnas.1403112111> PMID: 24812127
8. Güçlü U, van Gerven MAJ. Deep Neural Networks Reveal a Gradient in the Complexity of Neural Representations across the Ventral Stream. *The Journal of Neuroscience*. 2015; 35(27):10005–14. <https://doi.org/10.1523/JNEUROSCI.5023-14.2015> PMID: 26157000
9. Cichy RM, Khosla A, Pantazis D, Torralba A, Oliva A. Comparison of deep neural networks to spatio-temporal cortical dynamics of human visual object recognition reveals hierarchical correspondence. *Scientific Reports*. 2016; 6:27755. <https://doi.org/10.1038/srep27755> PMID: 27282108

10. Kriegeskorte N. Deep Neural Networks: A New Framework for Modeling Biological Vision and Brain Information Processing. *Annual Review of Vision Science*. 2015; 1(1):417–46. <https://doi.org/10.1146/annurev-vision-082114-035447> PMID: [28532370](https://pubmed.ncbi.nlm.nih.gov/28532370/)
11. Yamins DLK, DiCarlo JJ. Using goal-driven deep learning models to understand sensory cortex. *Nat Neurosci*. 2016; 19(3):356–65. <https://doi.org/10.1038/nn.4244> PMID: [26906502](https://pubmed.ncbi.nlm.nih.gov/26906502/)
12. Marr D. *Vision: A computational investigation into the human representation and processing of visual information*. San Francisco: WH Freeman; 1982.
13. DiCarlo James J, Zoccolan D, Rust Nicole C. How Does the Brain Solve Visual Object Recognition? *Neuron*. 2012; 73(3):415–34. <https://doi.org/10.1016/j.neuron.2012.01.010> PMID: [22325196](https://pubmed.ncbi.nlm.nih.gov/22325196/)
14. Carandini M. From circuits to behavior: a bridge too far? *Nat Neurosci*. 2012; 15(4):507–9. <https://doi.org/10.1038/nn.3043> PMID: [22449960](https://pubmed.ncbi.nlm.nih.gov/22449960/)
15. Heeger DJ. Theory of cortical function. *Proceedings of the National Academy of Sciences*. 2017; 114(8):1773–82. <https://doi.org/10.1073/pnas.1619788114> PMID: [28167793](https://pubmed.ncbi.nlm.nih.gov/28167793/)
16. Kay KN. Principles for models of neural information processing. *Neuroimage*. 2017. doi: <https://doi.org/10.1016/j.neuroimage.2017.08.016>.
17. Zeiler MD, Fergus R, editors. *Visualizing and understanding convolutional networks*. European conference on computer vision; 2014: Springer.
18. Yosinski J, Clune J, Nguyen A, Fuchs T, Lipson H. Understanding neural networks through deep visualization. arXiv preprint arXiv:150606579. 2015.
19. Bonner MF, Epstein RA. Coding of navigational affordances in the human visual system. *Proceedings of the National Academy of Sciences*. 2017; 114(18):4793–8. Epub April 17, 2017. <https://doi.org/10.1073/pnas.1618228114> PMID: [28416669](https://pubmed.ncbi.nlm.nih.gov/28416669/).
20. Epstein R, Kanwisher N. A cortical representation of the local visual environment. *Nature*. 1998; 392(6676):598–601. <https://doi.org/10.1038/33402> PMID: [9560155](https://pubmed.ncbi.nlm.nih.gov/9560155/)
21. Maguire EA. The retrosplenial contribution to human navigation: A review of lesion and neuroimaging findings. *Scand J Psychol*. 2001; 42(3):225–38. PMID: [11501737](https://pubmed.ncbi.nlm.nih.gov/11501737/)
22. Grill-Spector K. The neural basis of object perception. *Curr Opin Neurobiol*. 2003; 13(2):159–66. PMID: [12744968](https://pubmed.ncbi.nlm.nih.gov/12744968/)
23. Epstein RA, Higgins JS, Jablonski K, Feiler AM. Visual scene processing in familiar and unfamiliar environments. *J Neurophysiol*. 2007; 97(5):3670–83. <https://doi.org/10.1152/jn.00003.2007> PMID: [17376855](https://pubmed.ncbi.nlm.nih.gov/17376855/)
24. Epstein RA. Neural systems for visual scene recognition. In: Kveraga K, Bar M, editors. *Scene vision: making sense of what we see*. Cambridge, MA: MIT Press; 2014. p. 105–34.
25. Cichy RM, Khosla A, Pantazis D, Oliva A. Dynamics of scene representations in the human brain revealed by magnetoencephalography and deep neural networks. *Neuroimage*. 2017; 153:346–58. <https://doi.org/10.1016/j.neuroimage.2016.03.063> PMID: [27039703](https://pubmed.ncbi.nlm.nih.gov/27039703/)
26. Groen IIA, Greene MR, Baldassano C, Fei-Fei L, Beck DM, Baker CI. Distinct contributions of functional and deep neural network features to representational similarity of scenes in human brain and behavior. *eLife*. 2018; 7:e32962. <https://doi.org/10.7554/eLife.32962> PMID: [29513219](https://pubmed.ncbi.nlm.nih.gov/29513219/)
27. Gibson JJ. Visually controlled locomotion and visual orientation in animals. *Br J Psychol*. 1958; 49(3):182–94. <https://doi.org/10.1111/j.2044-8295.1958.tb00656.x> PMID: [13572790](https://pubmed.ncbi.nlm.nih.gov/13572790/)
28. Kriegeskorte N, Kievit RA. Representational geometry: integrating cognition, computation, and the brain. *Trends in Cognitive Sciences*. 2013; 17(8):401–12. Epub 2013/07/24. <https://doi.org/10.1016/j.tics.2013.06.007> PMID: [23876494](https://pubmed.ncbi.nlm.nih.gov/23876494/); PubMed Central PMCID: [PMC3730178](https://pubmed.ncbi.nlm.nih.gov/PMC3730178/).
29. Riesenhuber M, Poggio T. Hierarchical models of object recognition in cortex. *Nat Neurosci*. 1999; 2(11):1019–25. <https://doi.org/10.1038/14819> PMID: [10526343](https://pubmed.ncbi.nlm.nih.gov/10526343/)
30. Serre T, Oliva A, Poggio T. A feedforward architecture accounts for rapid categorization. *Proceedings of the National Academy of Sciences*. 2007; 104(15):6424–9. <https://doi.org/10.1073/pnas.0700622104> PMID: [17404214](https://pubmed.ncbi.nlm.nih.gov/17404214/)
31. Peirce JW. Understanding mid-level representations in visual processing. *Journal of Vision*. 2015; 15(7):5-. <https://doi.org/10.1167/15.7.5> PMID: [26053241](https://pubmed.ncbi.nlm.nih.gov/26053241/)
32. Nimom KF, Oswald FL. Understanding the Results of Multiple Linear Regression. *Organizational Research Methods*. 2013; 16(4):650–74. <https://doi.org/10.1177/1094428113493929>
33. Rajimehr R, Devaney KJ, Bilenko NY, Young JC, Tootell RBH. The "parahippocampal place area" responds preferentially to high spatial frequencies in humans and monkeys. *PLoS Biology*. 2011; 9(4).
34. Nasr S, Tootell RBH. A cardinal orientation bias in scene-selective visual cortex. *J Neurosci*. 2012; 32(43):14921–6. <https://doi.org/10.1523/JNEUROSCI.2036-12.2012> PMID: [23100415](https://pubmed.ncbi.nlm.nih.gov/23100415/)

35. Walther DB, Shen D. Nonaccidental Properties Underlie Human Categorization of Complex Natural Scenes. *Psychological Science*. 2014. <https://doi.org/10.1177/0956797613512662> PMID: [24474725](https://pubmed.ncbi.nlm.nih.gov/24474725/)
36. Nasr S, Echavarría CE, Tootell RBH. Thinking Outside the Box: Rectilinear Shapes Selectively Activate Scene-Selective Cortex. *The Journal of Neuroscience*. 2014; 34(20):6721–35. <https://doi.org/10.1523/JNEUROSCI.4802-13.2014> PMID: [24828628](https://pubmed.ncbi.nlm.nih.gov/24828628/)
37. Keil MS, Cristóbal G. Separating the chaff from the wheat: possible origins of the oblique effect. *J Opt Soc Am A*. 2000; 17(4):697–710. <https://doi.org/10.1364/JOSAA.17.000697>
38. Berman D, Golomb JD, Walther DB. Scene content is predominantly conveyed by high spatial frequencies in scene-selective visual cortex. *PLOS ONE*. 2017; 12(12):e0189828. <https://doi.org/10.1371/journal.pone.0189828> PMID: [29272283](https://pubmed.ncbi.nlm.nih.gov/29272283/)
39. Bryan PB, Julian JB, Epstein RA. Rectilinear Edge Selectivity Is Insufficient to Explain the Category Selectivity of the Parahippocampal Place Area. *Frontiers in Human Neuroscience*. 2016; 10(137). <https://doi.org/10.3389/fnhum.2016.00137> PMID: [27064591](https://pubmed.ncbi.nlm.nih.gov/27064591/)
40. Silson EH, Groen IIA, Kravitz DJ, Baker CI. Evaluating the correspondence between face-, scene-, and object-selectivity and retinotopic organization within lateral occipitotemporal cortex. *Journal of Vision*. 2016; 16(6):14-. <https://doi.org/10.1167/16.6.14> PMID: [27105060](https://pubmed.ncbi.nlm.nih.gov/27105060/)
41. Silson EH, Chan AW-Y, Reynolds RC, Kravitz DJ, Baker CI. A Retinotopic Basis for the Division of High-Level Scene Processing between Lateral and Ventral Human Occipitotemporal Cortex. *J Neurosci*. 2015; 35(34):11921–35. <https://doi.org/10.1523/JNEUROSCI.0137-15.2015> PMID: [26311774](https://pubmed.ncbi.nlm.nih.gov/26311774/)
42. Zhou B, Khosla A, Lapedriza A, Oliva A, Torralba A. Object detectors emerge in deep scene cnns. arXiv preprint arXiv:14126856. 2014.
43. Greene MR, Oliva A. The Briefest of Glances: The Time Course of Natural Scene Understanding. *Psychological Science*. 2009; 20(4):464–72. <https://doi.org/10.1111/j.1467-9280.2009.02316.x> PMID: [19399976](https://pubmed.ncbi.nlm.nih.gov/19399976/)
44. Choo H, Walther DB. Contour junctions underlie neural representations of scene categories in high-level human visual cortex. *Neuroimage*. 2016; 135:32–44. <https://doi.org/10.1016/j.neuroimage.2016.04.021> PMID: [27118087](https://pubmed.ncbi.nlm.nih.gov/27118087/)
45. Walther DB, Chai B, Caddigan E, Beck DM, Fei-Fei L. Simple line drawings suffice for functional MRI decoding of natural scene categories. *Proceedings of the National Academy of Sciences*. 2011; 108(23):9661–6.
46. Kornblith S, Cheng X, Ohayon S, Tsao DY. A network for scene processing in the macaque temporal lobe. *Neuron*. 2013; 79(4):766–81. Epub 2013/07/31. <https://doi.org/10.1016/j.neuron.2013.06.015> PMID: [23891401](https://pubmed.ncbi.nlm.nih.gov/23891401/).
47. Biederman I. Recognition-by-components: A theory of human image understanding. *Psychol Rev*. 1987; 94(2):115–47. <https://doi.org/10.1037/0033-295X.94.2.115> PMID: [3575582](https://pubmed.ncbi.nlm.nih.gov/3575582/)
48. Lescroart M, Gallant J. A model of surface depth and orientation predicts BOLD responses in human scene-selective cortex. *Journal of Vision*. 2015; 15(12):573-.
49. Cant JS, Xu Y. Object ensemble processing in human anterior-medial ventral visual cortex. *J Neurosci*. 2012; 32(22):7685–700. <https://doi.org/10.1523/JNEUROSCI.3325-11.2012> PMID: [22649247](https://pubmed.ncbi.nlm.nih.gov/22649247/)
50. Tsutsui K-I, Sakata H, Naganuma T, Taira M. Neural Correlates for Perception of 3D Surface Orientation from Texture Gradient. *Science*. 2002; 298(5592):409–12. <https://doi.org/10.1126/science.1074128> PMID: [12376700](https://pubmed.ncbi.nlm.nih.gov/12376700/)
51. Groen IIA, Silson EH, Baker CI. Contributions of low- and high-level properties to neural processing of visual scenes in the human brain. *Philosophical Transactions of the Royal Society B: Biological Sciences*. 2017; 372(1714). <https://doi.org/10.1098/rstb.2016.0102> PMID: [28044013](https://pubmed.ncbi.nlm.nih.gov/28044013/)
52. Mély DA, Serre T. Towards a Theory of Computation in the Visual Cortex. In: Zhao Q, editor. *Computational and Cognitive Neuroscience of Vision*. Singapore: Springer Singapore; 2017. p. 59–84.
53. Sharif Razavian A, Azizpour H, Sullivan J, Carlsson S. CNN features off-the-shelf: an astounding baseline for recognition. *Proceedings of the IEEE Conference on Computer Vision and Pattern Recognition Workshops 2014*. p. 806–13.
54. Yosinski J, Clune J, Bengio Y, Lipson H. How transferable are features in deep neural networks? *Advances in neural information processing systems 2014*. p. 3320–8.
55. Harel A, Kravitz DJ, Baker CI. Task context impacts visual object processing differentially across the cortex. *Proceedings of the National Academy of Sciences*. 2014; 111(10):E962–E71. <https://doi.org/10.1073/pnas.1312567111> PMID: [24567402](https://pubmed.ncbi.nlm.nih.gov/24567402/)
56. Charest I, Kievit RA, Schmitz TW, Deca D, Kriegeskorte N. Unique semantic space in the brain of each beholder predicts perceived similarity. *Proceedings of the National Academy of Sciences*. 2014; 111(40):14565–70. <https://doi.org/10.1073/pnas.1402594111> PMID: [25246586](https://pubmed.ncbi.nlm.nih.gov/25246586/)

57. Marchette SA, Vass LK, Ryan J, Epstein RA. Outside Looking In: Landmark Generalization in the Human Navigational System. *The Journal of Neuroscience*. 2015; 35(44):14896–908. <https://doi.org/10.1523/JNEUROSCI.2270-15.2015> PMID: [26538658](https://pubmed.ncbi.nlm.nih.gov/26538658/)
58. Julian JB, Fedorenko E, Webster J, Kanwisher N. An algorithmic method for functionally defining regions of interest in the ventral visual pathway. *Neuroimage*. 2012; 60(4):2357–64. <https://doi.org/10.1016/j.neuroimage.2012.02.055> PMID: [22398396](https://pubmed.ncbi.nlm.nih.gov/22398396/)
59. Stolier RM, Freeman JB. Neural pattern similarity reveals the inherent intersection of social categories. *Nat Neurosci*. 2016; 19(6):795–7. <https://doi.org/10.1038/nn.4296> PMID: [27135216](https://pubmed.ncbi.nlm.nih.gov/27135216/)
60. Garcia D. Robust smoothing of gridded data in one and higher dimensions with missing values. *Computational Statistics & Data Analysis*. 2010; 54(4):1167–78.
61. Goslee SC, Urban DL. The ecodist Package for Dissimilarity-based Analysis of Ecological Data. *Journal of Statistical Software*. 2007; 22(7):1–19. <https://doi.org/10.18637/jss.v022.i07>
62. Nili H, Wingfield C, Walther A, Su L, Marslen-Wilson W, Kriegeskorte N. A Toolbox for Representational Similarity Analysis. *PLOS Computational Biology*. 2014; 10(4):e1003553. <https://doi.org/10.1371/journal.pcbi.1003553> PMID: [24743308](https://pubmed.ncbi.nlm.nih.gov/24743308/)
63. van der Maaten L, Hinton G. Visualizing data using t-SNE. *Journal of Machine Learning Research*. 2008; 9(Nov):2579–605.
64. Greene MR, Oliva A. Recognition of natural scenes from global properties: Seeing the forest without representing the trees. *Cognit Psychol*. 2009; 58(2):137–76. <https://doi.org/10.1016/j.cogpsych.2008.06.001> PMID: [18762289](https://pubmed.ncbi.nlm.nih.gov/18762289/)